Science Advances
AAAS

# Supplementary Materials for

## A long-life lithium-oxygen battery via a molecular quenching/ mediating mechanism

Jinqiang Zhang, Yufei Zhao, Bing Sun*, Yuan Xie, Anastasia Tkacheva, Feilong Qiu, Ping He, Haoshen Zhou, Kang Yan, Xin Guo, Shijian Wang, Andrew M. McDonagh, Zhangquan Peng*, Jun Lu*, Guoxiu Wang*

*Corresponding author. Email: bing.sun@uts.edu.au (B.S.); zqpeng@dicp.ac.cn (Z.P.); junlu@anl.gov (J.L.); guoxiu.wang@uts.edu.au (G.W.)

Published 21 January 2022, *Sci. Adv.* **8**, eabm1899 (2022)
DOI: 10.1126/sciadv.abm1899

**The PDF file includes:**

Figs. S1 to S45
Table S1
Legend for movie S1

**Other Supplementary Material for this manuscript includes the following:**

Movie S1

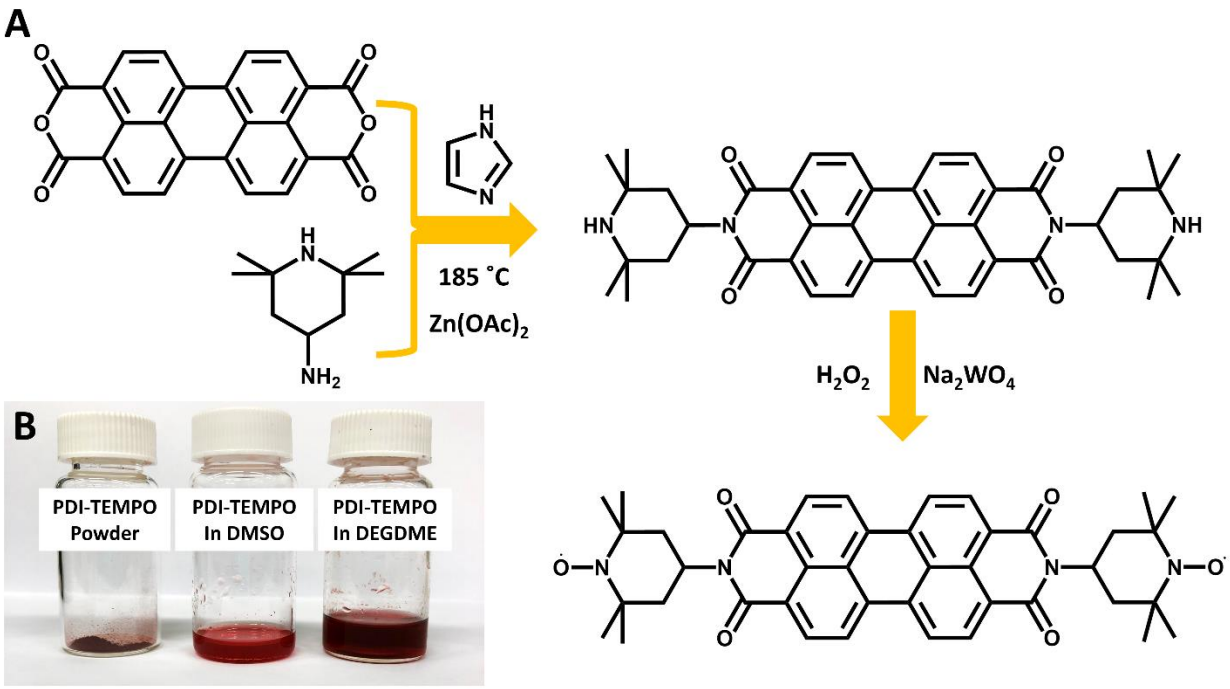


**Fig. S1. The synthesis of PDI-TEMPO. A.** Schematic illustration of the synthesis approach of PDI-TEMPO. **B.** The physical appearance of the as-synthesized PDI-TEMPO powder (left), the PDI-TEMPO/DMSO solution (middle), and the PDI-TEMPO/DEGDME solution (right).

The as-synthesis PDI-TEMPO has a purple-red colour. Interestingly, the colours of the PDI-TEMPO solutions are slightly different when using different organic solvents. The DMSO solution appears to be red, while the DEGDME solution has a colour close to purple. Furthermore, the colour of the solution gradually changes to pink when lowing the concentration.

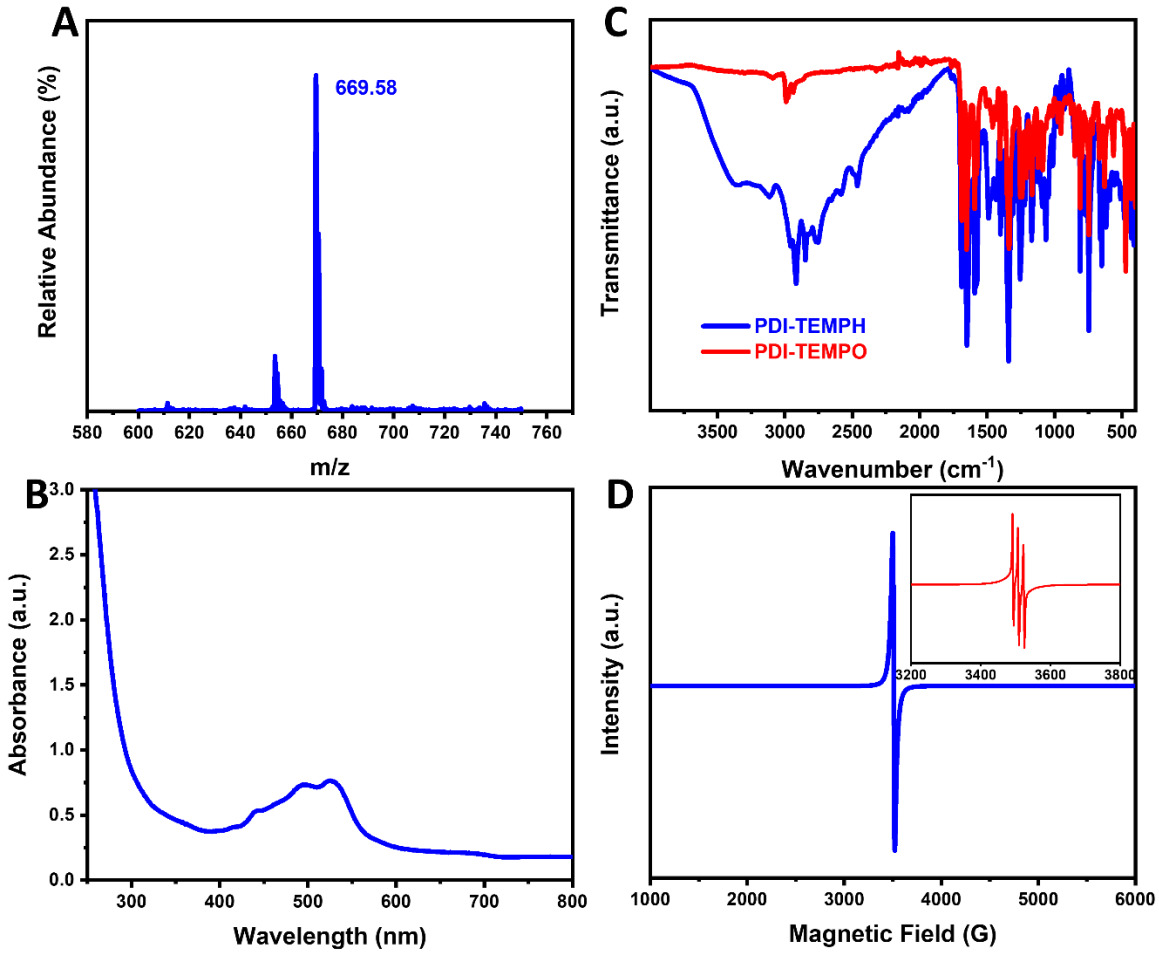


**Fig. S2. Characterizations of PDI-TEMPH and PDI-TEMPO. A.** The mass spectrometry of the PDI-TEMPH. **B.** The UV spectrum of the PDI-TEMPO in DMSO solvent. **C.** The FTIR spectra of the PDI-TEMPH and PDI-TEMPO. **D.** The EPR spectra of the PDI-TEMPO in solid-state and DMSO solution (inset).

The mass spectrometry was performed on PDI-TEMPH instead of the final radical product PDI-TEMPO, as the free radicals may affect the spectrometry result. As shown in Fig. S2A, the strongest peak at 669.58 refers to the molecular mass of PDI-TEMPH (668+1), demonstrating the successful synthesis of the precursor PDI-TEMPH. The FTIR spectra of both PDI-TEMPH and PDI-TEMPO show high peak intensity around 1650 and 1680 $cm^{-1}$, corresponding to the amide groups (*50*). The peaks related to N-H groups disappears in the one of PDI-TEMPO, indicating that the N-H groups are oxidized into N-O radical groups. The UV spectrum in Fig. S2B shows the characteristic peaks of perylene diimide. Furthermore, the EPR spectra of PDI-TEMPO prove the existence of N-O free radicals. Therefore, it can be concluded that PDI-TEMPO is successfully synthesized.

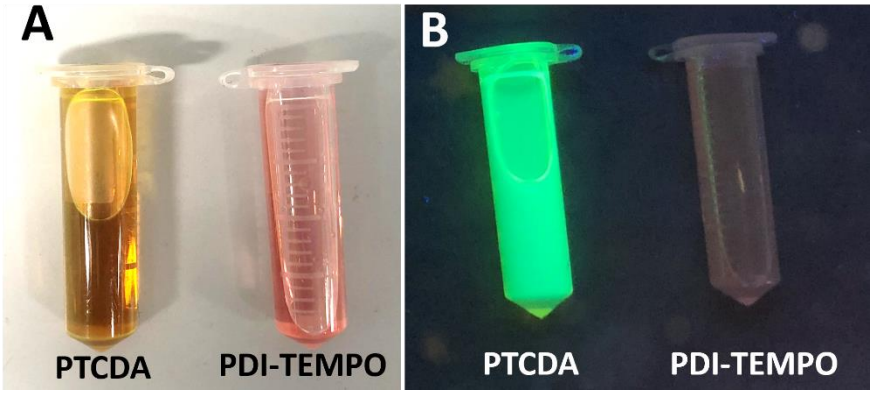


**Fig. S3. The quenching of the fluorescence capability of PDI backbone.** The PTCDA/water solution and PDI-TEMPO/DMSO solution under **A.** the normal light and **B.** UV light.

The precursor PTCDA was dissolved in KOH solution, due to its insolubility in most organic solvents. PDI-TEMPO was dissolved in DMSO as it could not be dissolved in the aqueous media. As shown in Fig. S3B, the precursor showed strong fluorescence emission, owing to the large conjugated PDI backbone. Interestingly, the existence of TEMPO free radicals in the molecular structure could efficiently quench the fluorescence capability of the PDI backbone (*44*). It further confirms the successful grafting of TEMPO on PDI backbone.

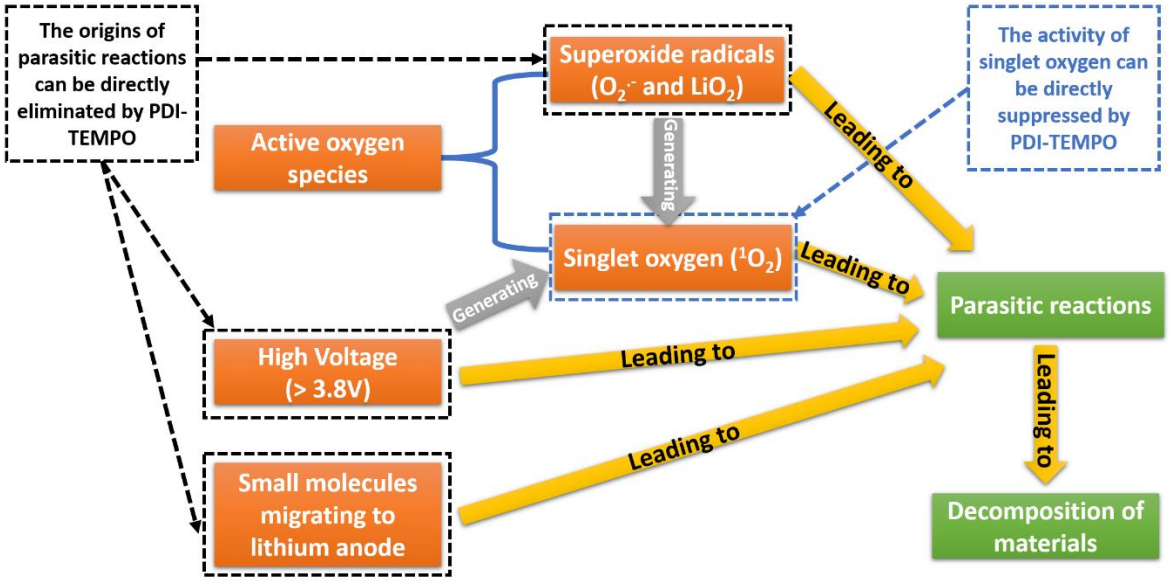


**Fig. S4. The illustration of PDI-TEMPO to comprehensive suppress parasitic reactions.** The decomposition mechanisms of materials use yellow arrows and the origins of singlet oxygen use gray arrows.

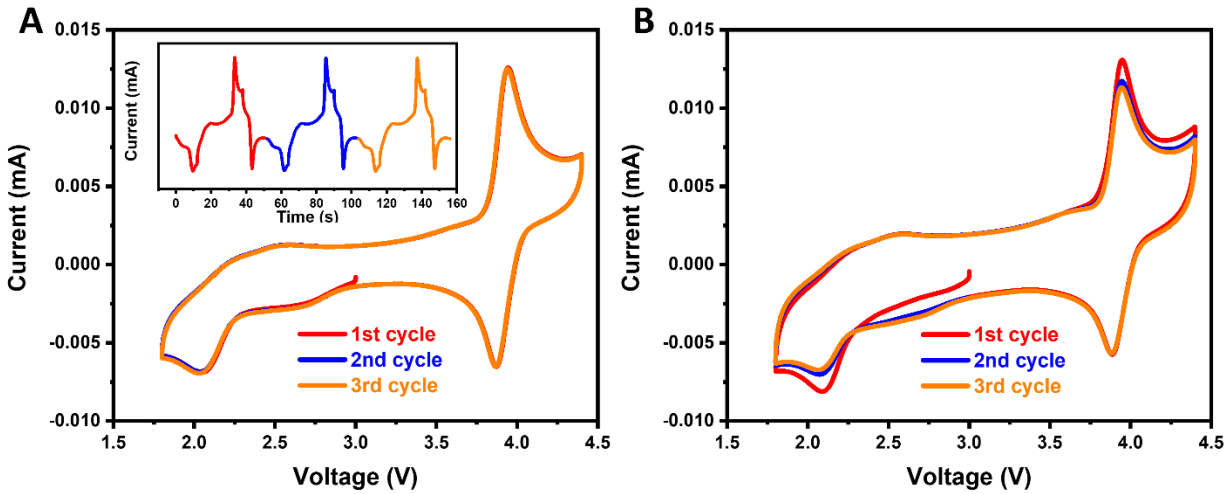


**Fig. S5. CV curves of three-electrode cells with PDI-TEMPO in an argon atmosphere A. before and B. after 25 cycles scan in an oxygen atmosphere.** The inset image is the curve of current vs. time. The scan rate is 100 mV $s^{-1}$.

As shown in Fig. S5B, the redox behaviors are similar to those before cycling (Fig. S5A). The slight difference between the first cycle and the following cycle is probably due to the remaining $Li_2O_2/O_2$ in the electrode/electrolyte during the scanning in oxygen. But the curves of the second and third cycles are almost identical, verifying the redox reactions are still highly reversible after cycling. This verifies that the PDI-TEMPO molecule is highly stable during cycling.

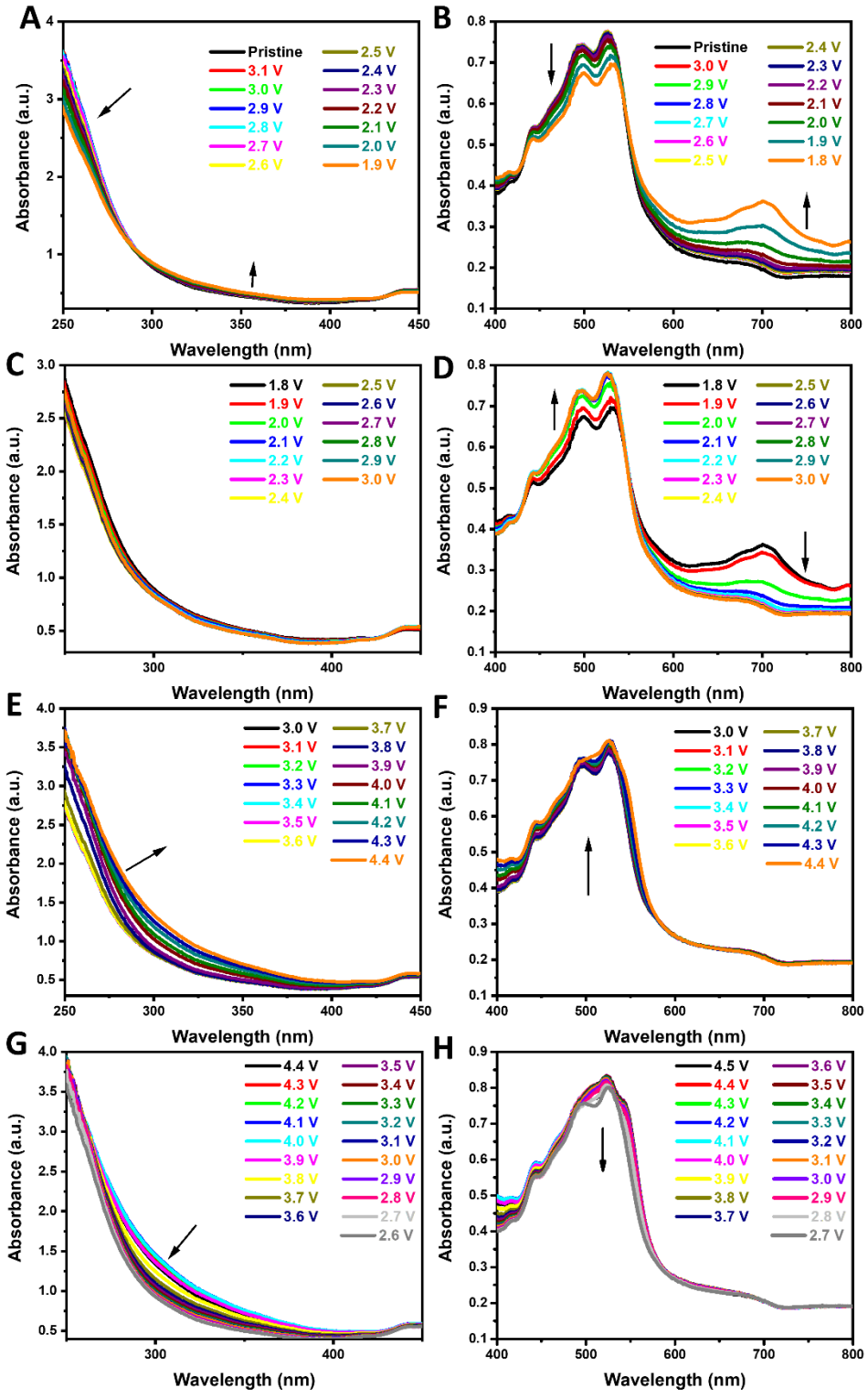


**Fig. S6. The UV spectra of the PDI-TEMPO/DEGDME electrolyte during the *in-situ* tests.** The voltage range was set to **A-B.** 3.1-1.9 V, **C-D.** 1.9-3.1 V, **E-F.** 3.1-4.5 V, **G-H.** 4.5-2.7 V.

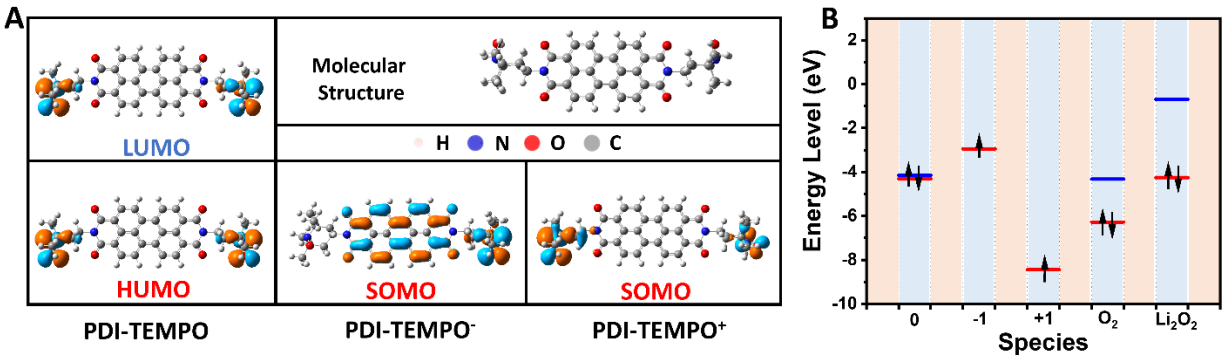


**Fig. S7. DFT calculations of the redox capabilities of PDI-TEMPO molecules and the catalytic activity towards the activation of oxygen. A.** DFT calculation of the visualized LUMO and HOMO/SOMO of PDI-TEMPO at different oxidation states, and **B.** their corresponding energy comparing to the $O_2$ and $Li_2O_2$. The blue lines are the LUMO of the molecules, and the red lines are the HOMO/SOMO of the molecules. 0 refers to the neutral PDI-TEMPO, -1 refers to the reduced PDI-TEMPO (PDI-TEMPO$^-$), and +1 refers to the oxidized PDI-TEMPO (PDI-TEMPO$^+$). Arrows represent the electrons spinning in the orbitals.

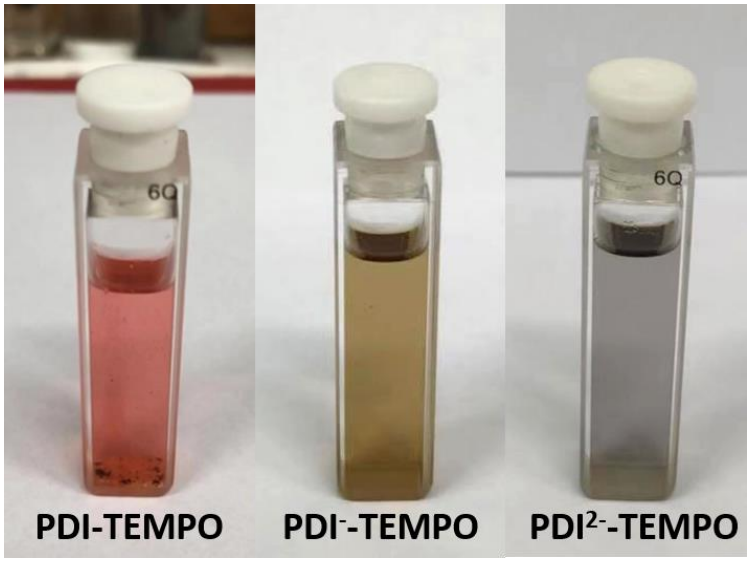


**Fig. S8. The digital photos of the PDI-TEMPO/DMSO solution at different reduction stage.**

The reduction of the PDI backbone was controlled by adding different amount of $KO_2$ in the PDI-TEMPO/DMSO solution. As shown in Fig. S8, the original PDI-TEMPO displays a red colour. The solution changed to brown and light blue when the PDI backbone was reduced into -1 and -2, respectively (*41*). The result indicates that the PDI backbone could be reduced by superoxide radicals in the solution.

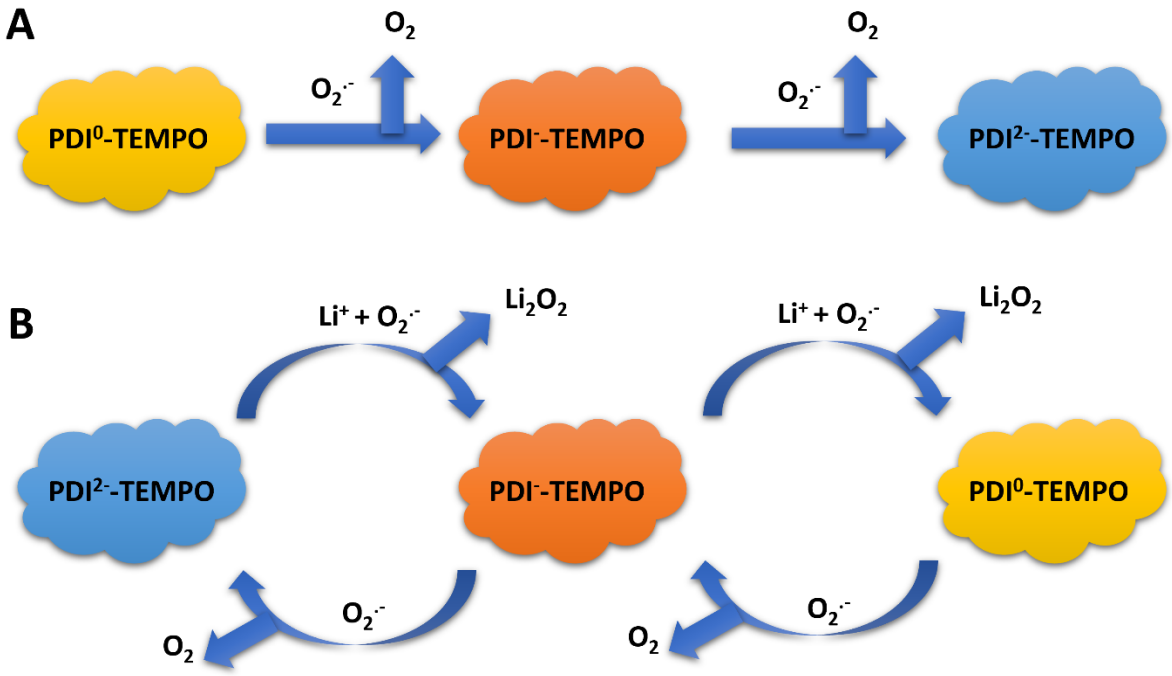


**Fig. S9. The chemical reactions in the electrolyte with $KO_2$ with the addition of A. PDI-TEMPO and then B. lithium salt.**

As shown in Fig. S9A, the PDI backbone can be easily reduced by superoxide radicals to $PDI^{\cdot-}$-TEMPO and $PDI^{2-}$-TEMPO. However, after the addition of lithium salt in the solution, the reactions between PDI backbone and superoxide become complicated. The reduced $PDI^{\cdot-}$-TEMPO and $PDI^{2-}$-TEMPO can be reversibly oxidized by superoxide with the aid of lithium salt. Whereas, the existence of superoxide in the system can still reduce the neutral PDI-TEMPO and $PDI^{\cdot-}$-TEMPO. As a result, the reduction and oxidation occur at the same time in the electrolyte after the addition of lithium salt, leading to the mixture of these species instead of pure neutral PDI-TEMPO at the original state.

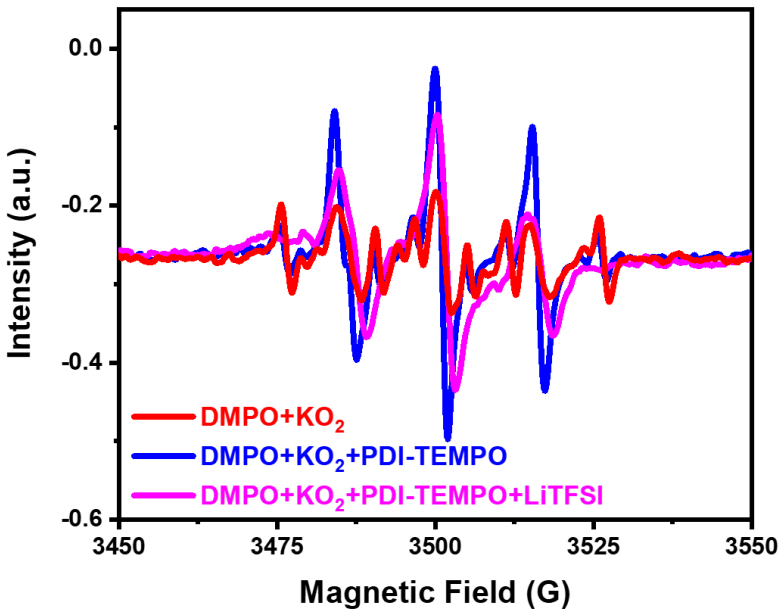


**Fig. S10. EPR spectra of the superoxide-saturated solution before and after adding PDI-TEMPO and LiTFSI.**

The intensities of the peaks related to the existence of superoxide radicals trapped by 5,5-dimethyl-1-pyrroline N-oxide (DMPO) decreased when PDI-TEMPO was added to the solution. The peaks vanished when LiTFSI was also added. This indicates that the superoxide radicals could be efficiently quenched by PDI-TEMPO with the aid of lithium salt.

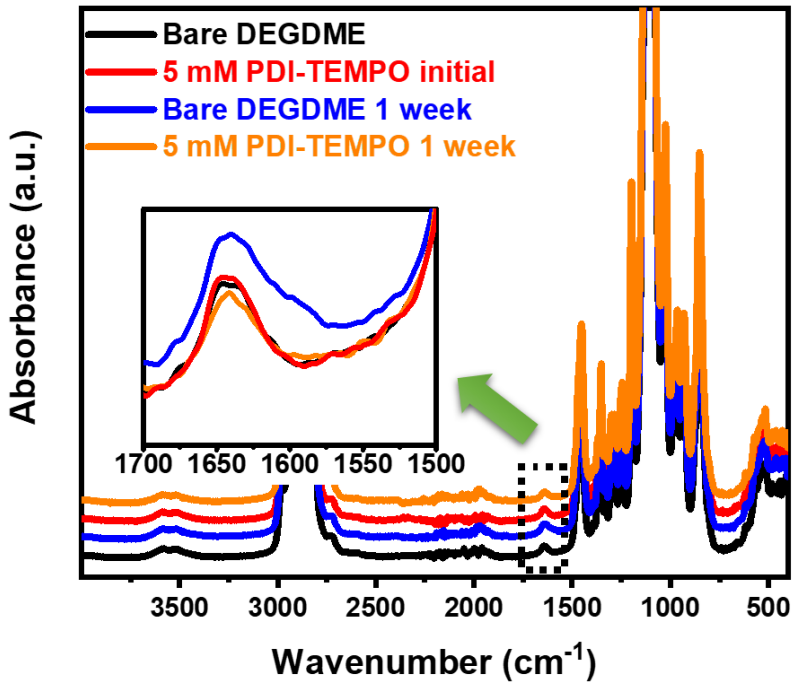


**Fig. S11. FTIR spectra of the $KO_2$-soaked DEGDME solutions with and without PDI-TEMPO after one week.** The inset figure is the enlarged image of the stacked spectra in the range of 1500-1700 $cm^{-1}$.

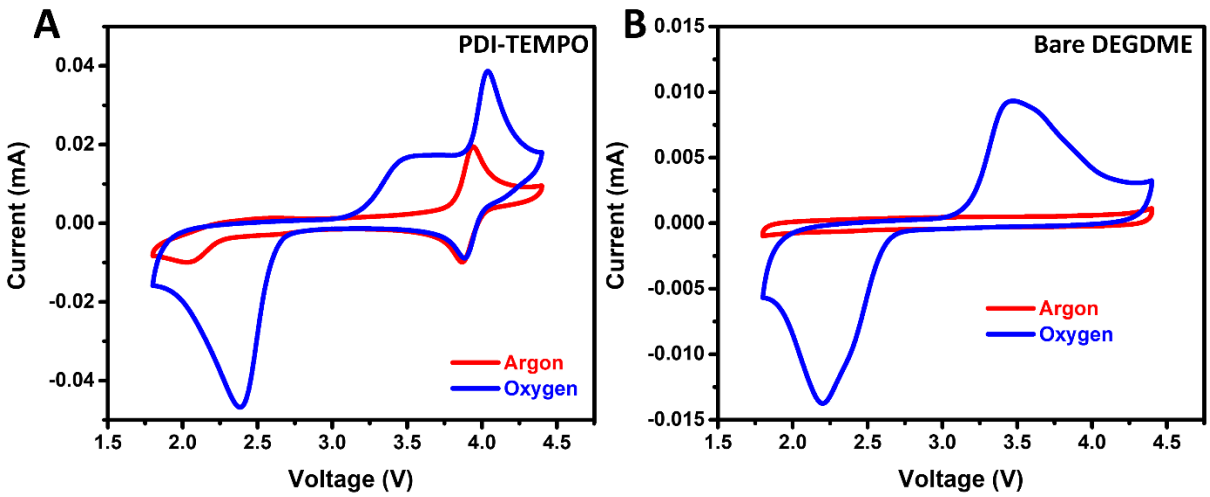


**Fig. S12. The CV curves of the three-electrode cells operated in the argon and oxygen atmosphere with different electrolyte: A.** PDI-TEMPO electrolyte and **B.** bare DEGDME electrolyte. The scan rate is 100 mV $s^{-1}$.

The currents related to ORR and OER when operated in PDI-TEMPO electrolyte are significantly higher than those obtained in DEGDME electrolyte, indicates that the existence of PDI-TEMPO could efficiently enhance the ORR and OER process simultaneously.

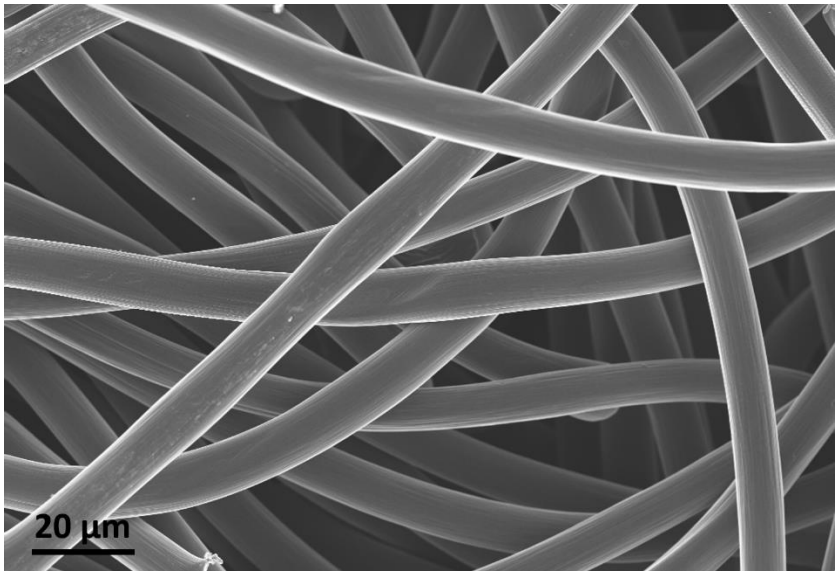


**Fig. S13. SEM image of the carbon paper electrode.**

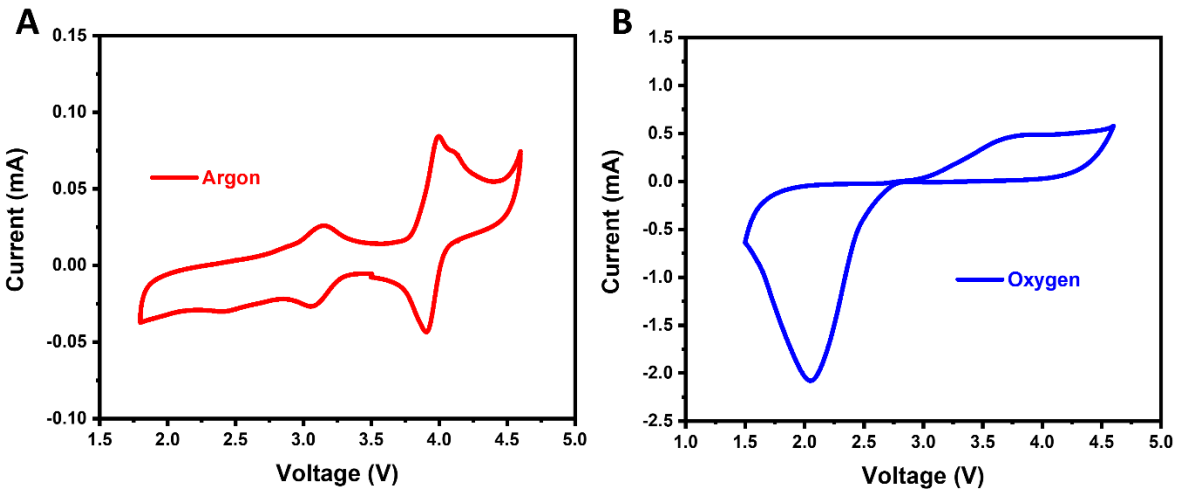


**Fig. S14. The CV curves of the two-electrode cells with PDI-TEMPO electrolyte operated in A. the argon atmosphere and B. the oxygen atmosphere.** The scan rate is 0.5 mV $s^{-1}$.

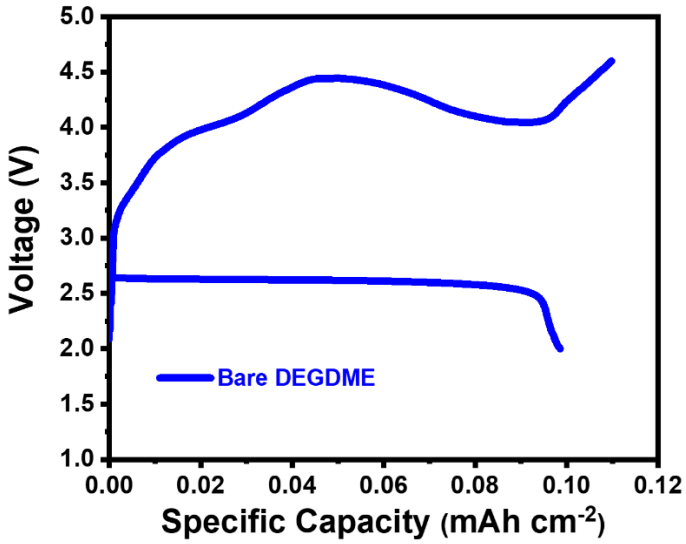


**Fig. S15. The discharge-charge profiles of the cell with bare DEGDME electrolyte in the oxygen atmosphere.** It is the enlarged image from Fig. 2A. The current density is 0.1 mA $cm^{-2}$, and the cut-off voltage is set to 2.0/4.6 V.

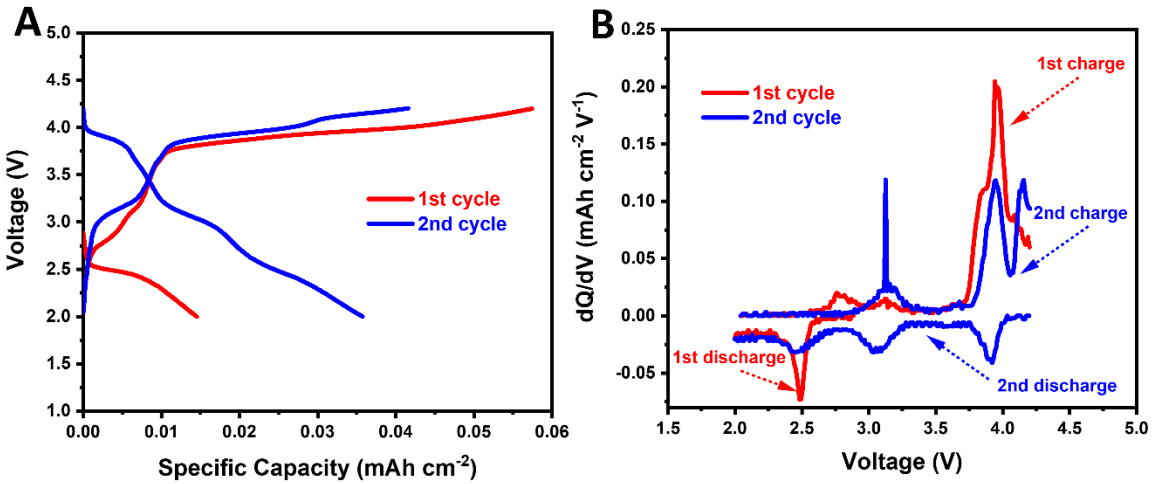


**Fig. S16. The discharge-charge profiles of the cell with PDI-TEMPO electrolyte in the argon atmosphere.** The current density is 0.1 mA $cm^{-2}$, and the cut-off voltage is set to 2.0/4.2 V.

The cell with PDI-TEMPO electrolyte operated in the argon atmosphere could provide capacity of less than 0.04 mA $cm^{-2}$. Furthermore, the calculated dQ/dV *vs.* V shows similar curves to the CV results in Fig. 1C, referring to the reversible chemical reactions of PDI-TEMPO.

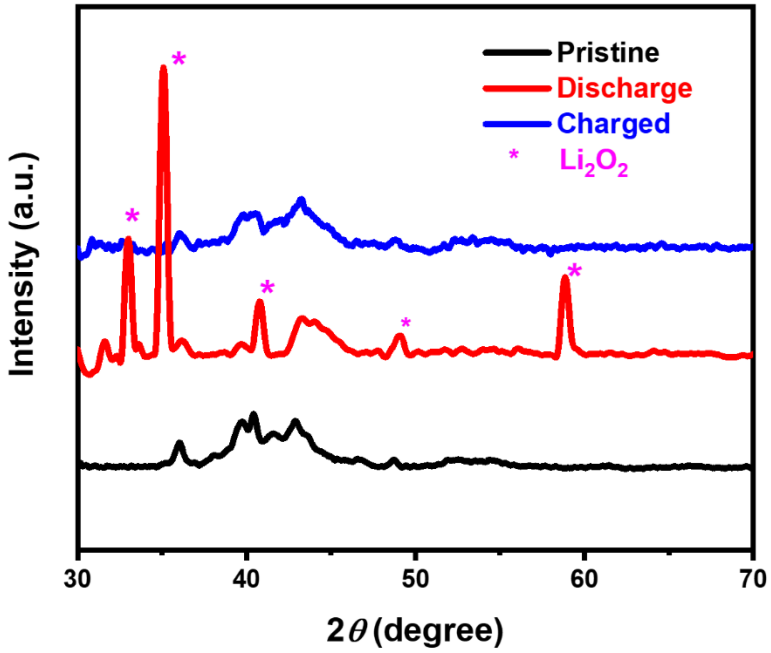


**Fig. S17. The XRD patterns of the carbon paper electrodes before and after the first cycle.**

The XRD pattern of the discharged electrode indicates that the discharge product was dominated by $Li_2O_2$. The peaks disappeared after the charge process, demonstrating highly reversible formation and decomposition of $Li_2O_2$ during the operation of Li-$O_2$ batteries.

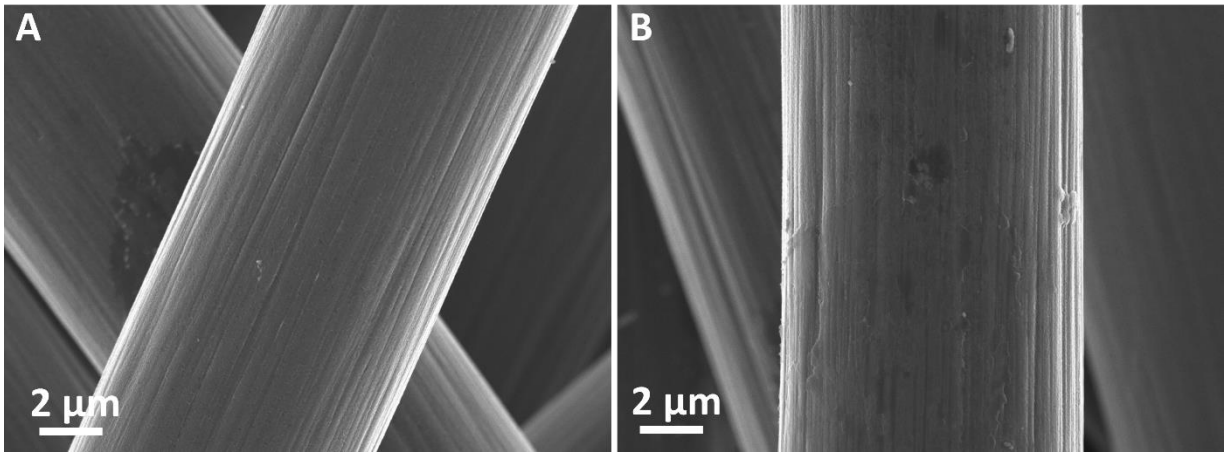


**Fig. S18. The SEM images of the charged carbon paper electrode with A. PDI-TEMPO electrolyte and B. DEGDME electrolyte.**

The SEM images show that no residue discharge products left on the charged carbon paper, indicating $Li_2O_2$ has been completely decomposed during the charge process.

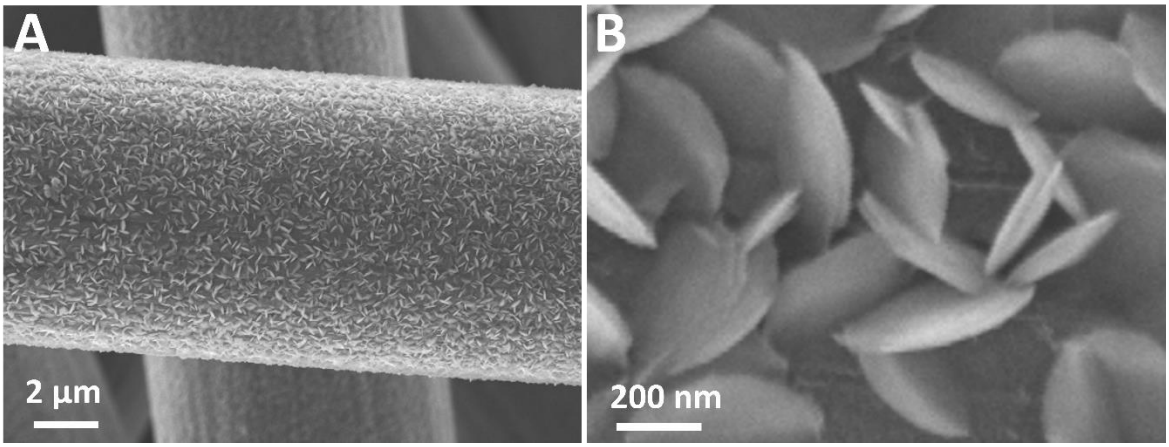


**Fig. S19. The SEM images of the discharge carbon paper electrode with a DEGDME electrolyte containing 2000 ppm water.**

The electrolyte was prepared by adding 2000 ppm water to enable solution-mediated discharge process. As shown in Fig. S19, the carbon fibres are covered with large $Li_2O_2$ particles in toroidal shapes with a diameter of around 400-500 nm, which is consistent with most publications (*52*). There are also no particles found amongst the toroidal-shaped $Li_2O_2$.

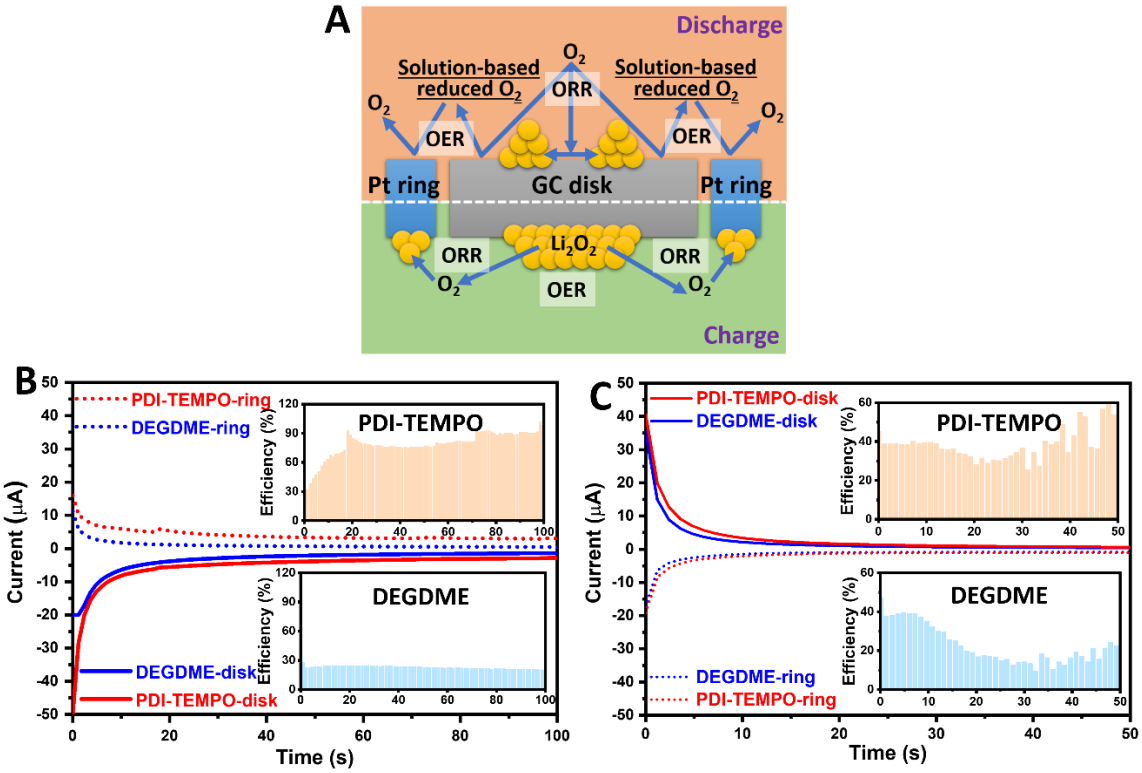


**Fig. S20. The RRDE curves of the three-electrode cells simulated for B. discharge (in $O_2$) and C. charge (in Ar) processes, and A. the schematic illustration of the reaction mechanisms.** The reduction voltage was set to 2.3 V *vs.* Li/Li$^+$, and the oxidation voltage was set to 4.1 V *vs.* Li/Li$^+$. The electrolyte was prepared by dissolving 0.5 mM PDI-TEMPO in DEGDME electrolyte containing 0.5 M LiTFSI. The inset images are the efficiencies calculated by the corrected equations in Experimental session and Fig. S21.

A demonstration rotating ring-disk electrode (RRDE) measurement was further conducted to reveal the nature of reactions. A home-made three-electrode cell was applied with a Pt wire as the counter electrode and a Ag wire as the reference electrode. The discharge process was simulated by applying a reduction potential to the disk electrode and an oxidation potential to the ring electrode in the oxygen atmosphere. The charge process was simulated by applying an oxidation potential to the disk electrode and a reduction potential to the ring electrode in the argon atmosphere, directly after the simulated discharge process. During the simulated discharge process, the current generated on the glassy carbon disk electrode originates from the ORR process, and the current on the Pt ring electrode is from the reduction of the solution-based reduced $O_2$ species (Fig. S20A). During the simulated charge process, the current generated on the glassy carbon disk electrode comes from the OER process by decomposing the pre-generated $Li_2O_2$, and the current on the Pt ring electrode refers to the reduction of the released $O_2$ from OER on disk electrode (Fig. S20A). As shown in Fig. S20B, the current generated on disk electrode in PDI-TEMPO electrolyte was significantly higher than that in DEGDME electrolyte, revealing that the addition of PDI-TEMPO could dramatically facilitate the discharge process. As the discharge product $Li_2O_2$ is insoluble in the electrolytes, the currents gradually decreased with time due to the continuous coverage of the active surface of the disk electrode. Similarly during the simulated charge process (Fig. S20C), the currents generated in the PDI-TEMPO electrolyte were higher

than that in DEGDME electrolyte. The currents decreased with time due to the exhaustion of the $Li_2O_2$ accumulated during the simulated discharge process. The discharge and charge mechanisms could be estimated by calculating the Faradaic efficiency (calculation details in the Experimental section and Fig. S21). As shown in the inset images in Fig. S20, the calculated Faradaic efficiency in PDI-TEMPO electrolyte increase rapidly from the initial 35 % to almost 100 % during the continuous scans, while the calculated Faradaic efficiency in DEGDME electrolyte reaches 30 % initially but dropped quickly to 25 % with time. It provides direct evidence that the discharge process in PDI-TEMPO electrolyte was dominated by the solution-based mechanism, since more solution-based intermediates were generated. Furthermore, the higher Faradaic efficiency in PDI-TEMPO electrolyte during the simulated charge process is much higher and persistent than DEGDME electrolyte, indicating a high charge efficiency when PDI-TEMPO was present in the electrolyte (inset images in Fig. S20C).

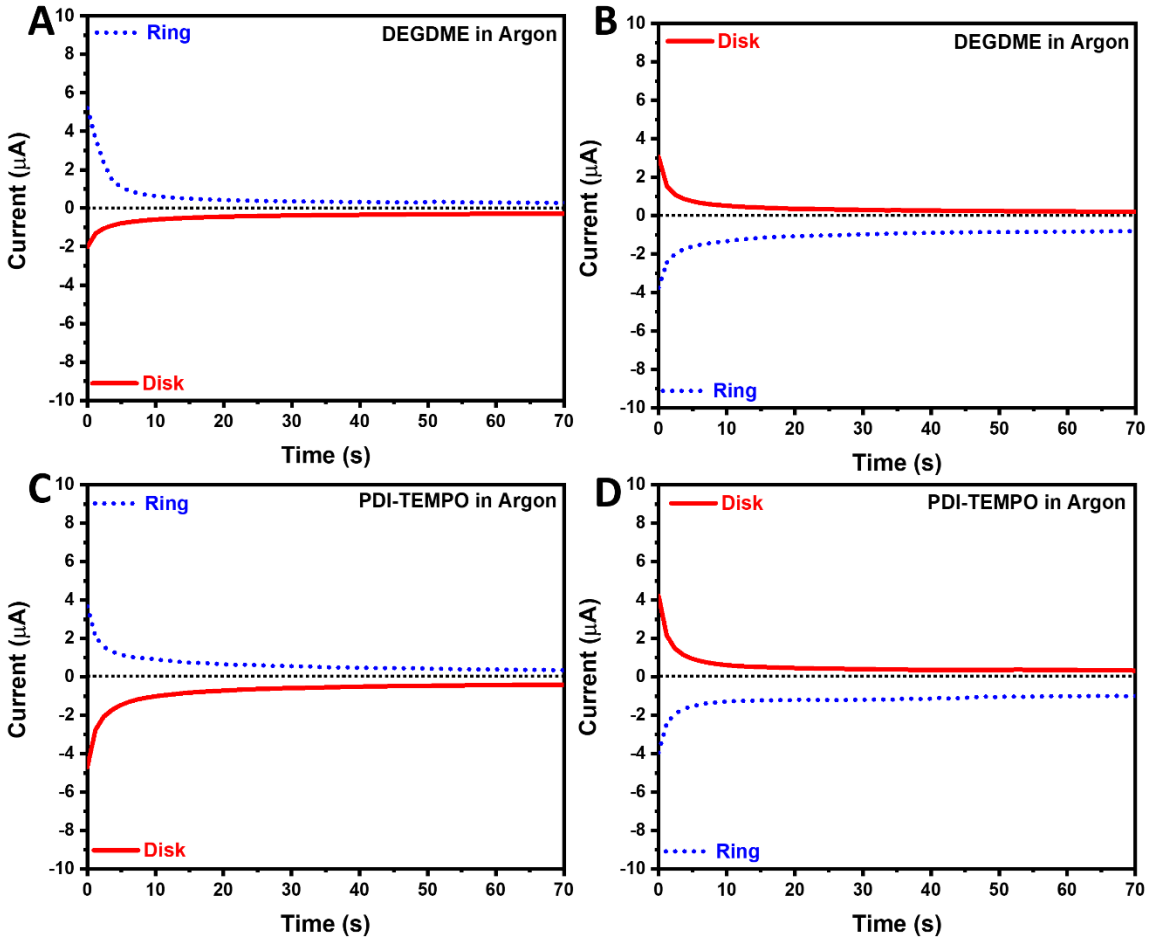


**Fig. S21. RRDE curves control experiment using of A-B. DEGDME electrolyte and C-D. PDI-TEMPO electrolyte in the argon atmosphere.** The reduction voltage was set to 2.3 V *vs.* $Li/Li^+$, and the oxidation voltage was set to 4.1 V *vs.* $Li/Li^+$. The electrolyte was prepared by dissolving 0.5 mM PDI-TEMPO in DEGDME electrolyte containing 0.5 M LiTFSI.

The conduct of this control experiment was performed in the argon atmosphere. Therefore, the current densities obtained on the disk and ring electrode should only originate from the side-reactions and redox reactions of PDI-TEMPO. Therefore, in order to obtain the accurate efficiency result of oxygen consumption and generation, the equation to calculate the efficiency should be corrected as follows:

$$Efficiency = (I_{ring} - I_{ring-correction})/(I_{disk} - I_{disk-correction})$$

The $I_{ring}$ and $I_{disk}$ are the currents obtained on the ring and disk electrode during the ORR and OER process. The $I_{ring\text{-}correction}$ and $I_{disk\text{-}correction}$ are the currents obtained on the ring and disk electrodes during the control experiment. In this way, the efficiencies calculated based on this corrected equation could function as indicators of the discharge and charge efficiency.

Interestingly, both currents generated on the Pt ring electrode at the reduction voltage (2.3 V *vs.* $Li/Li^+$) were significantly higher than the ones obtained at oxidation voltage (4.1 V *vs.* $Li/Li^+$) or those generated on the glassy carbon disk electrode. That is to say, the side reactions mainly occurred on the Pt ring electrode during the reduction scan, and under other circumstances, the side reactions were negligible.

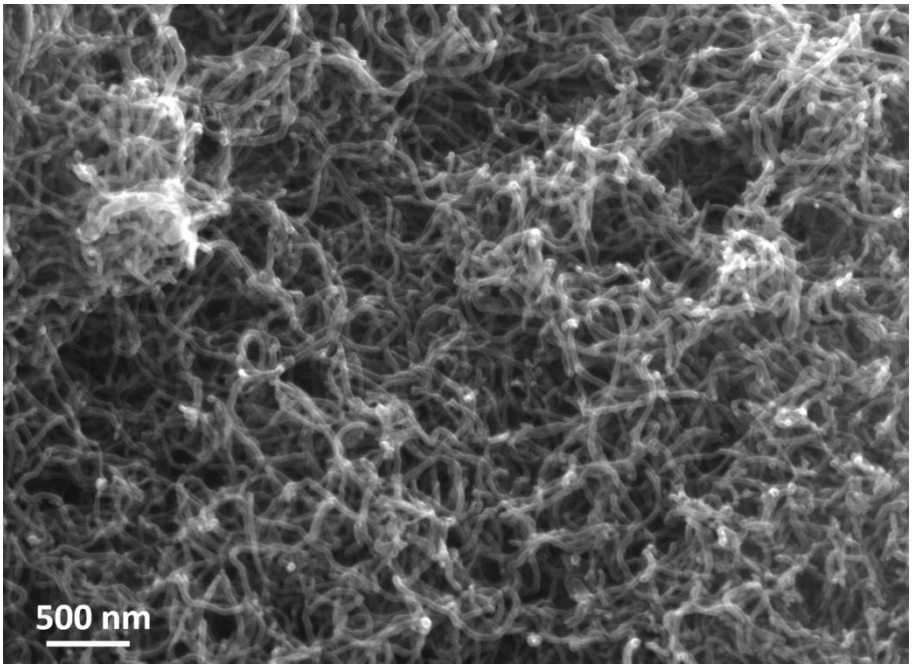


**Fig. S22. SEM image of the CNT electrode.**

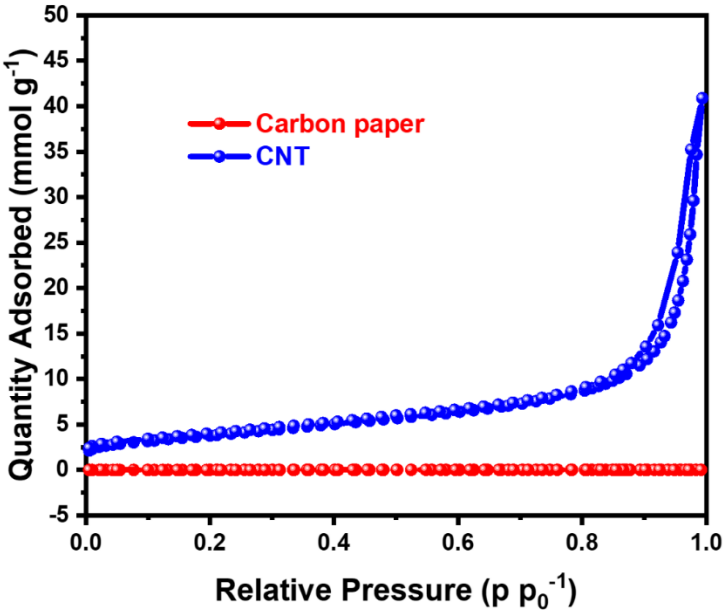


**Fig. S23. BET results of the carbon paper and CNT.**

The BET area of carbon paper is 0.984 $m^2 g^{-1}$ and The BET surface area of CNT is 315.12 $m^2 g^{-1}$. Moreover, the pore volume of CNT (0.4526 $cm^3 g^{-1}$) is more than 100 times of carbon paper (0.0042 $cm^3 g^{-1}$). Therefore, the replacement of carbon paper with CNT should generate higher discharge capacity when bare DEGDME electrolyte is used, which should provide more insight by comparing it with the PDI-TEMPO electrolyte.

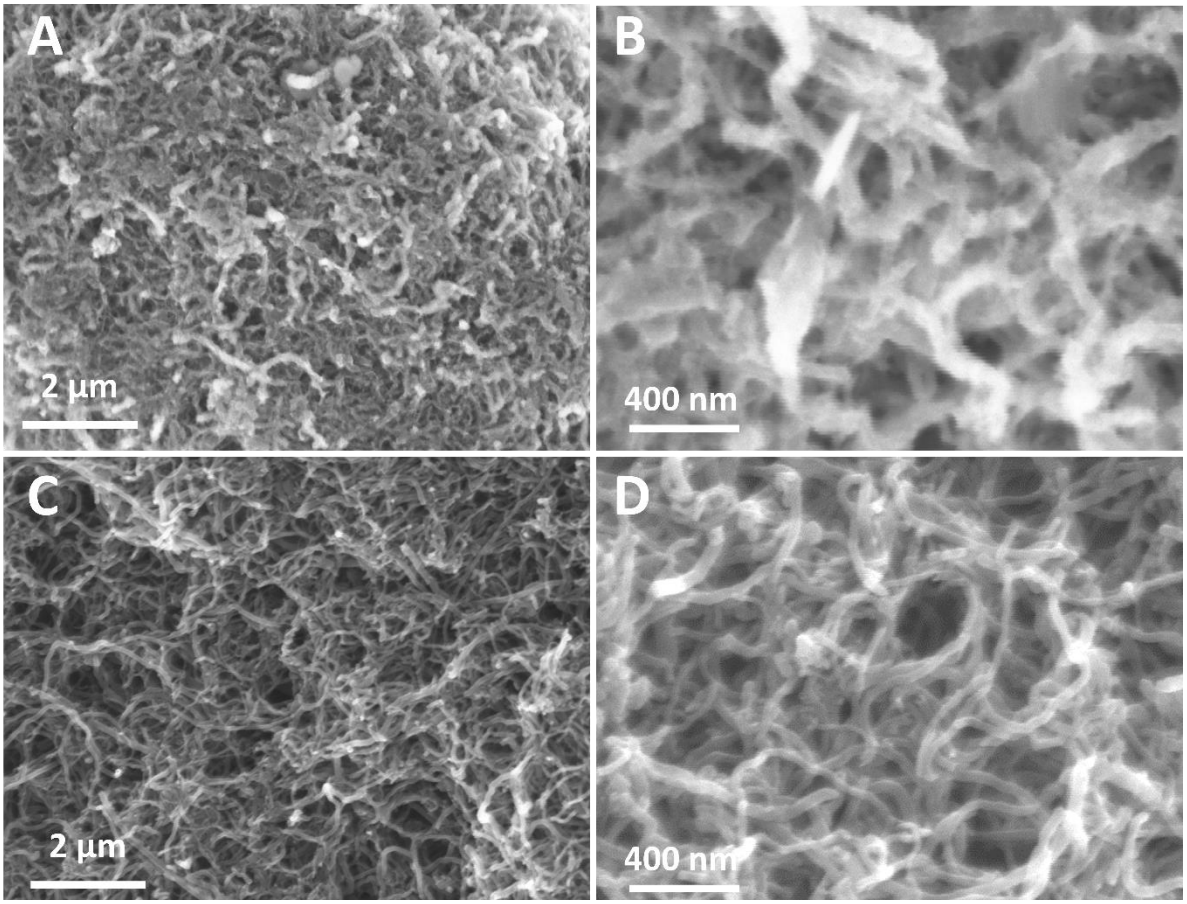


**Fig. S24. The SEM images of CNT electrode after A-B. discharge process and C-D. charge process with PDI-TEMPO electrolyte.** **B** is the enlarged image of **A**, and **D** is the enlarged image of **C**.

The SEM image of the CNT electrode after the discharge process with PDI-TEMPO electrolyte shows a large number of nanoparticles formed on CNTs instead of common toroidal-shape plates. This proves that the discharge process in PDI-TEMPO proceeds through a different mechanism from the conventional solution-mediated route. As the formed $Li_2O_2$ were in small nanoparticles, it is reasonable to assume that the discharge process was dominated by the chemical disproportion reaction of the superoxide radicals. The $Li_2O_2$ nanoparticles completely disappeared after the charge process, indicating the formation/decomposition of nanosized $Li_2O_2$ is highly reversible.

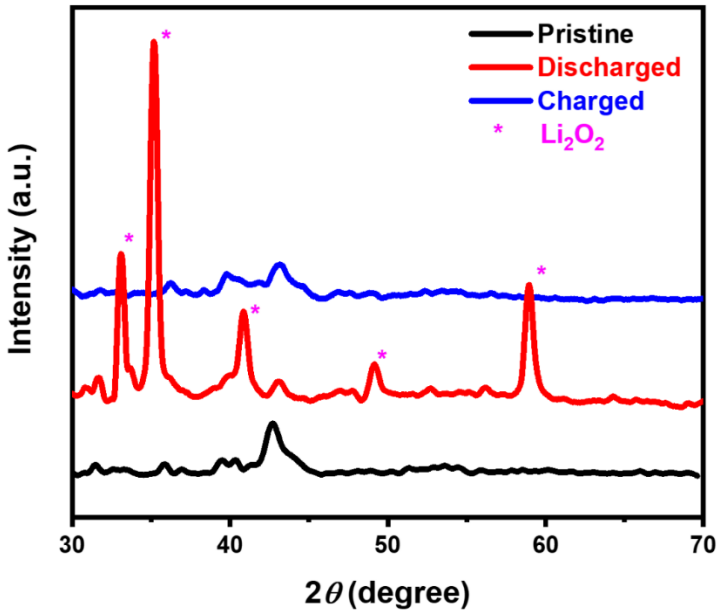


**Fig. S25. The XRD patterns of the CNT electrodes before and after the first cycle.**

The XRD pattern of the discharged electrode indicates that the discharge product was dominated by $Li_2O_2$. The peaks disappeared after the charge process, demonstrating highly reversible formation and decomposition of $Li_2O_2$ during the operation of Li-$O_2$ batteries.

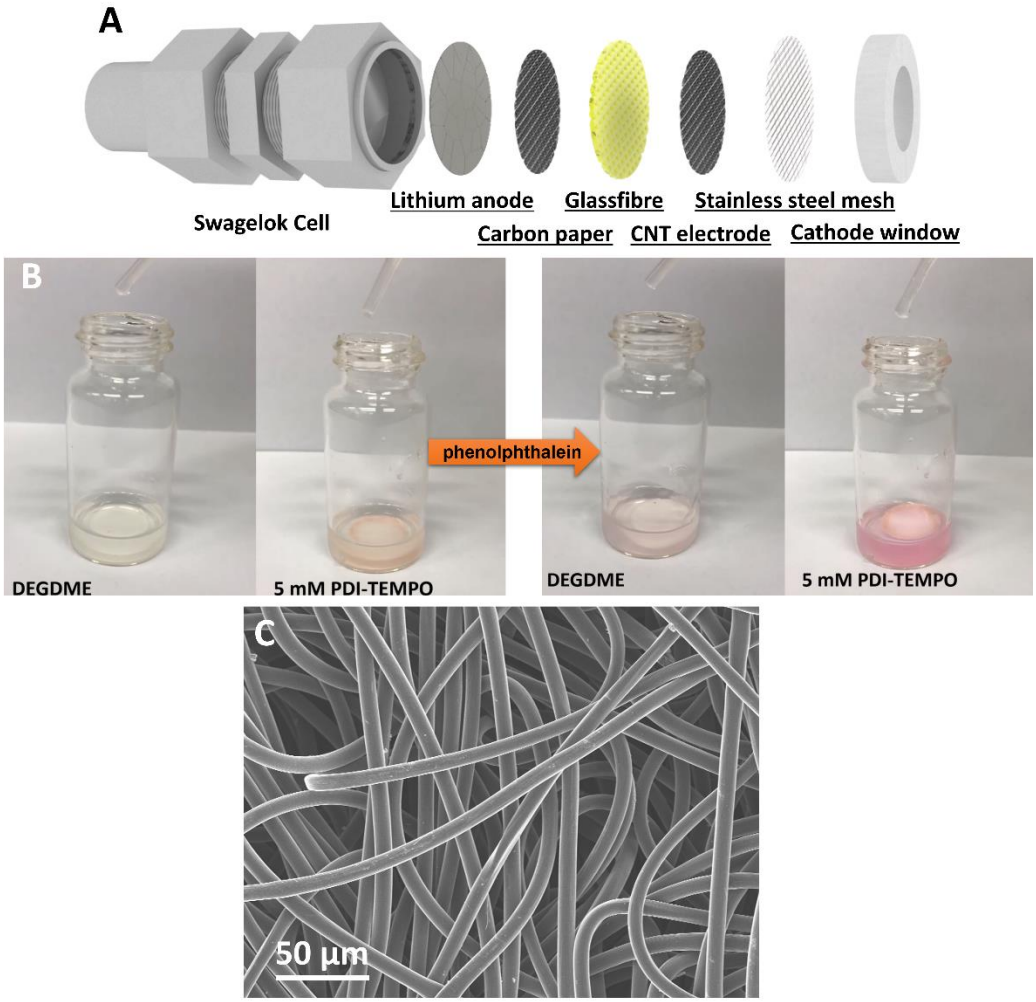


**Fig. S26. The demonstration experiment to prove that the discharge process was mainly accelerated by the chemical disproportion of superoxide radicals.** **A.** The special cell configuration containing an additional carbon paper between the lithium anode and separator. **B.** The demonstration experiment by adding phenolphthalein into the glassfibre/aqueous electrolyte. **C.** The SEM image of the carbon paper between lithium anode and separator.

The chemical disproportion of superoxide radicals in the electrolyte led to the scattering of $Li_2O_2$ particles in the cathode and on one side of separator next to the cathode. It was confirmed by adding phenolphthalein to the solution which was prepared by soaking glassfibre in water. The scattered particles reacted to water to form an alkaline solution, which was confirmed by phenolphthalein (turning pink, Fig. S26B and Supplementary Video). This proves that the particles scattered in separator were $Li_2O_2$. This demonstration experiment confirms that a small quantity of $Li_2O_2$ would be scattered into the electrolyte and deposited on the separator during the discharge process, and this should only originate from the chemical disproportion reaction of the superoxides in the electrolyte. Furthermore, there are no particles spotted on the carbon paper on the other side of the separator, indicating that the $Li_2O_2$ are mainly scattered on one side of the separator close to the cathode (Fig. S26C).

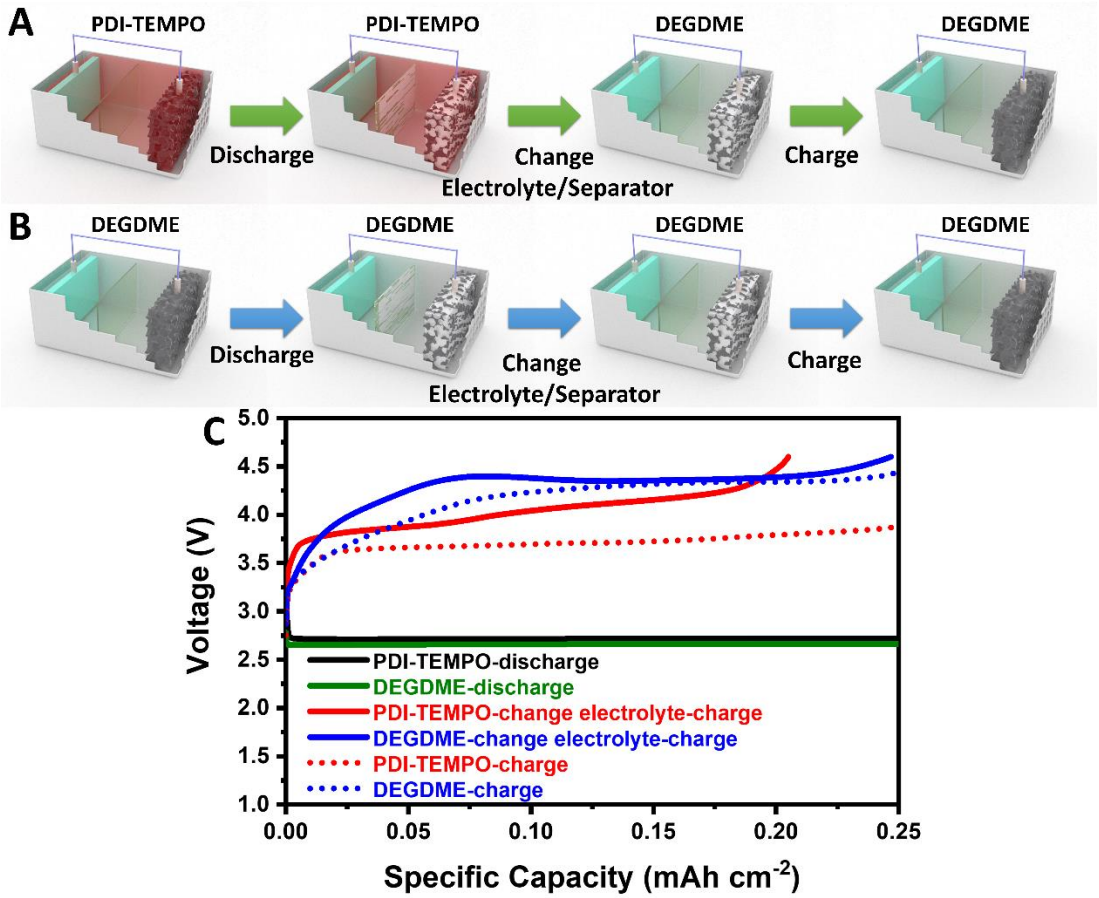


**Fig. S27. The demonstration experiment to prove the scattering of $Li_2O_2$ in the separator during the discharge process with PDI-TEMPO electrolyte.** The schematic illustration of the changing of separator/electrolyte after discharge in **A.** PDI-TEMPO electrolyte and **B.** DEGDME electrolyte. **C.** The discharge-charge profiles of the Li-$O_2$ cells with and without the changing of separator/electrolyte after discharge. The cells were discharged with a current density of 0.1 mA $cm^{-2}$. The used separators/electrolytes were taken out and changed to the fresh separator/DEGDME electrolyte. The cells were then charged to a cut-off voltage of 4.6 V. The discharge-charge processes were also performed without the changing of separator/electrolyte.

The change of the separator/electrolyte after discharge in PDI-TEMPO electrolyte has caused the loss of about 20 % capacity fade, comparing to the DEGDME electrolyte. It indicates that a small quantity of $Li_2O_2$ was scattered to the electrolyte and separator, proving the discharge process was dominated by chemical disproportion reaction of superoxides. Furthermore, as shown in the charge curves in Fig. S27, the charge over-potential of the PDI-TEMPO cell with the changed electrolyte was still lower than the one in DEGDME electrolyte, even without the effect of redox mediator. This also confirms that the small-sized particles were easier to be decomposed than the toroidal-shaped $Li_2O_2$, further demonstrating the beneficial effect with the superoxide radical quencher in the electrolyte.

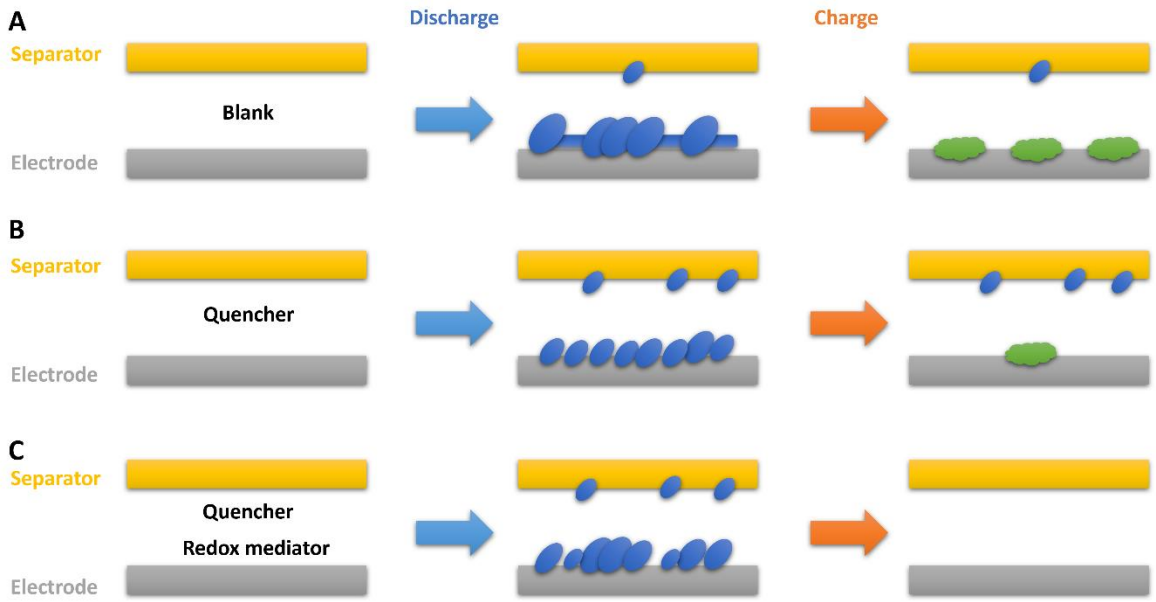


**Fig. S28. The schematic illustration of the discharge-charge processes with different additives in the electrolyte: A.** blank electrolyte, **B.** electrolyte with quencher, and **C.** electrolyte with quencher/redox mediator.

The discharge process in DEGDME electrolyte was mainly dominated by the electrochemical reaction route. Therefore, $Li_2O_2$ spotted in the bare DEGDME electrolyte can be mainly found in the cathode (Fig. S28A). The addition of superoxide radical quencher in the electrolyte would result in not only the formation of small-sized $Li_2O_2$ particles, but also the scattering of $Li_2O_2$ to one side of separator close to cathode (Fig. S28B). This phenomenon is beneficial to increasing the discharge capacity and may lower the charge over-potentials in the subsequent charge process. However, it also induced an additional problem that the scattered $Li_2O_2$ on the separator could not be easily decomposed as the separator was usually insulator. Therefore, this problem could be eliminated as the redox mediator could function as a mobile charge carrier, which could efficiently decompose the scattered $Li_2O_2$ on the separator (Fig. S28C). Therefore, PDI-TEMPO, which combines the function of a superoxide radical quencher and a redox mediator, is ideal for the use in Li-$O_2$ batteries with enhanced electrochemical performance.

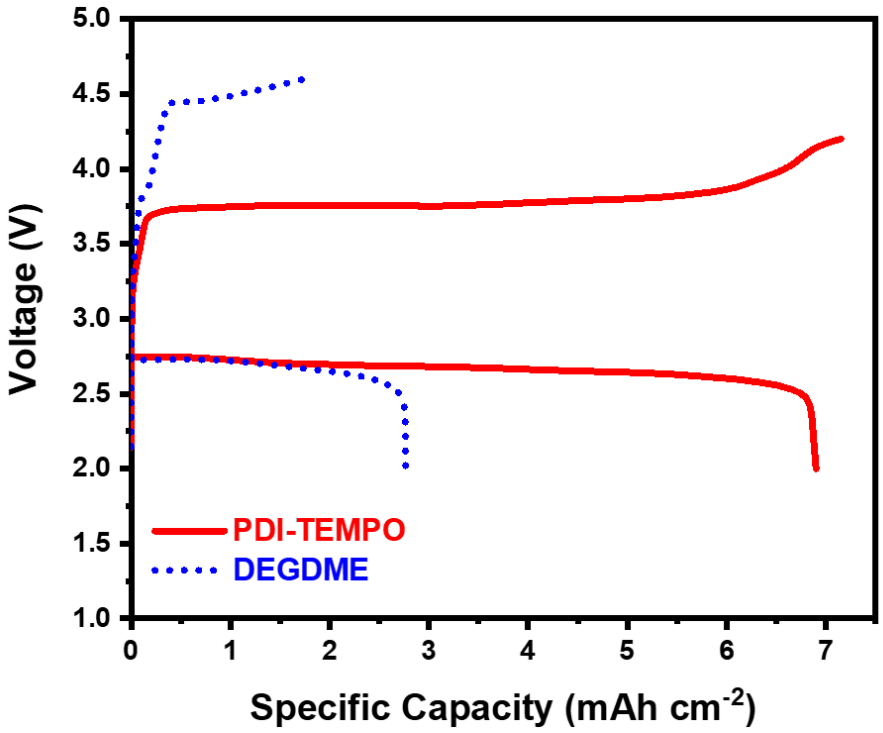


**Fig. S29. The full discharge-charge profiles of the Li-$O_2$ cells with different electrolytes using CNT electrodes.** The current density is 0.1 mA $cm^{-2}$, and the cut-off voltage is set to 2.0/4.6 V.

The addition of PDI-TEMPO in the electrolyte could efficiently enhance the capacity and lower the charge over-potentials when using CNT electrodes.

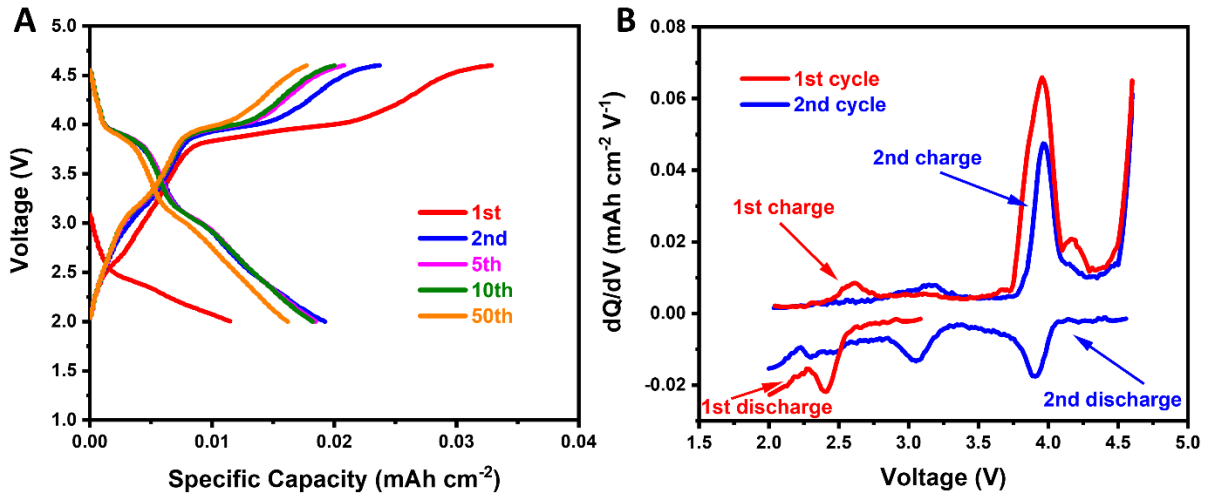


**Fig. S30. A. The discharge-charge profiles of the cells with PDI-TEMPO electrolyte in argon atmosphere using the CNT electrodes and B. the corresponding dQ/dV *vs.* V.** The current density is 0.1 mA $cm^{-2}$, and the cut-off voltage is set to 2.0/4.6 V.

The reversible capacity was lower than 0.2 mAh $cm^{-2}$ in the argon atmosphere, which is negligible compared to the capacity in Fig. S29.

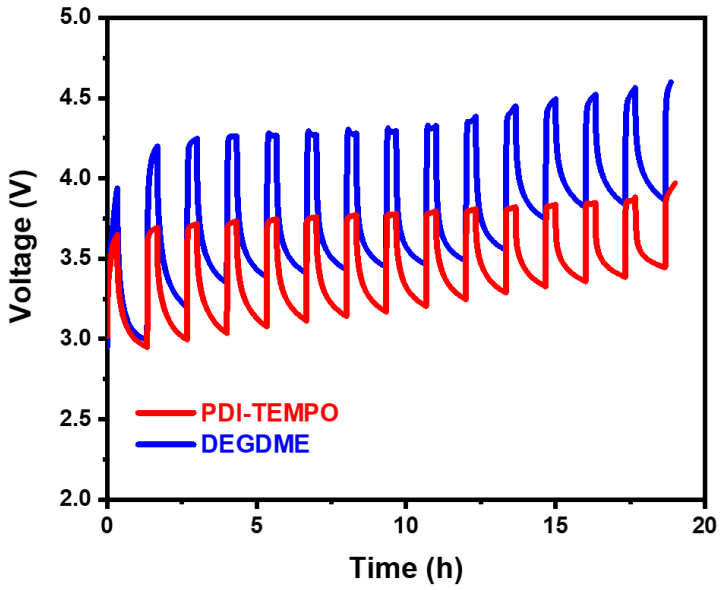


**Fig. S31. GITT curves of the Li-$O_2$ cells, which were acquired with a current density of 0.1 mA $cm^{-2}$ for 0.5 mAh $cm^{-2}$ and a 60 min time interval during the discharge and charge processes.**

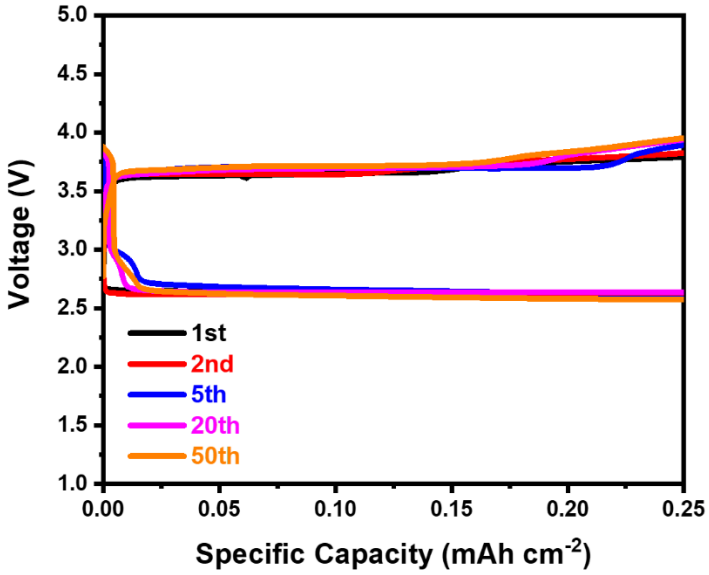


**Fig. S32. The cycling performance of the Li-$O_2$ cells with PDI-TEMPO electrolyte using carbon paper electrodes.**

The electrochemical performance indicates that the addition of PDI-TEMPO could efficiently enhance the discharge and charge processes, and also maintain an excellent cycling performance.

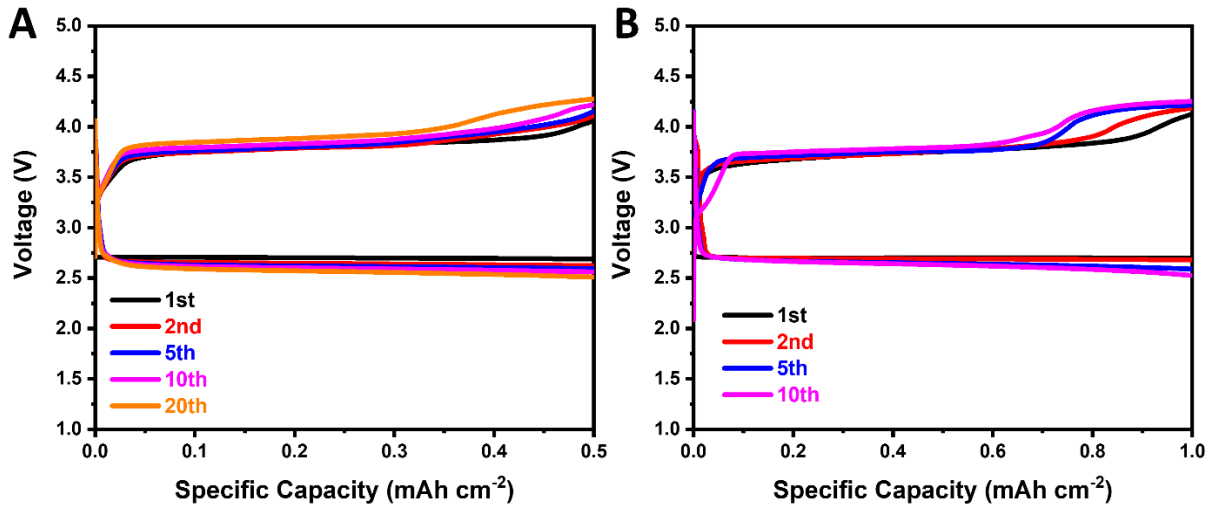


**Fig. S33. The discharge-charge profiles of Li-$O_2$ cells with PDI-TEMPO electrolyte using CNT electrodes at different cut-off capacity: A.** 0.5 mAh $cm^{-2}$, and **B.** 1 mAh $cm^{-2}$. The current density is 0.1 mA $cm^{-2}$.

The Li-$O_2$ batteries could still maintain good cycling performance when the reversible cut-off capacities were extended to 0.5 mAh $cm^{-2}$ and 1 mAh $cm^{-2}$.

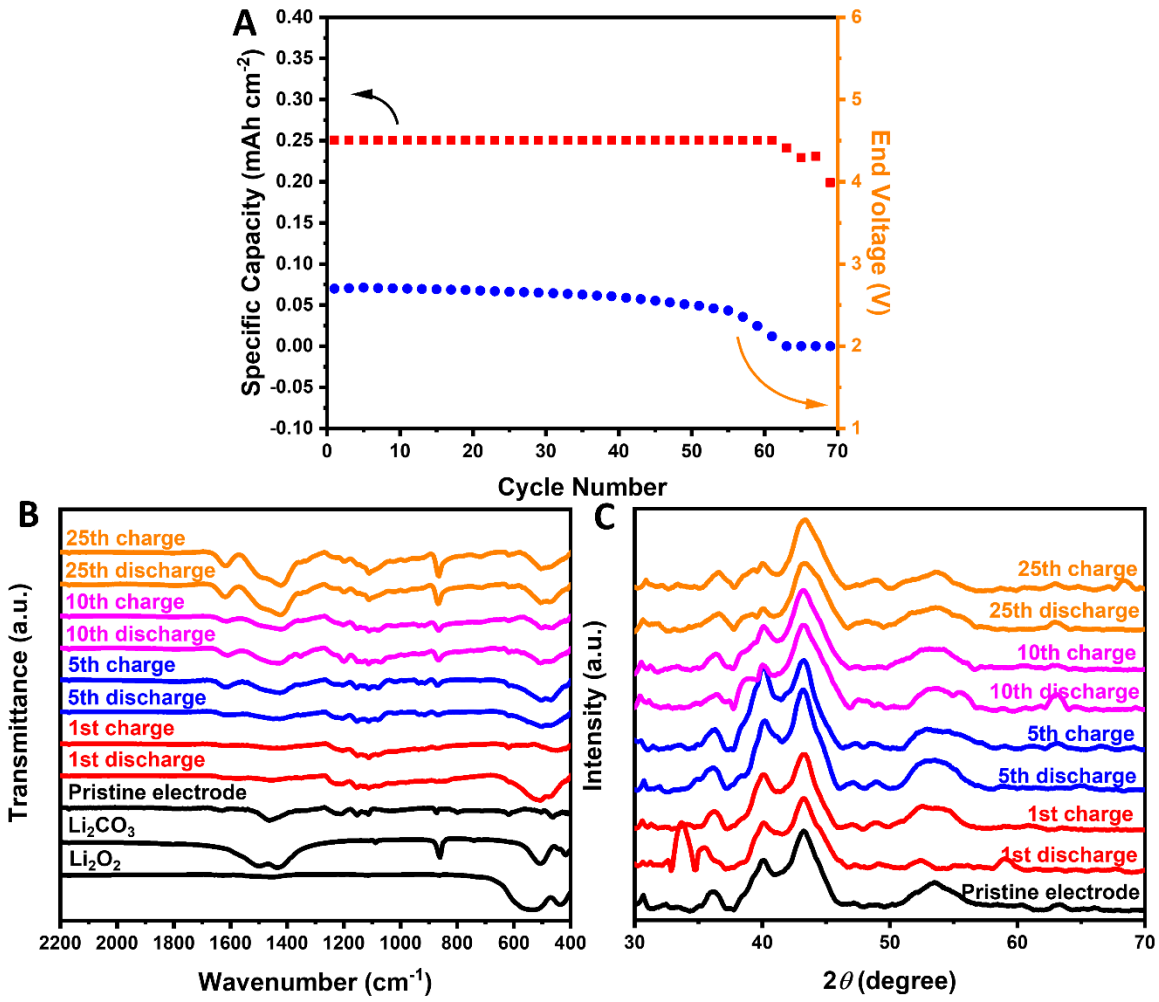


**Fig. S34. The post-mortem characterization of Li-$O_2$ batteries with TEMPO electrolyte after cycles: A.** The cycling performance of the Li-$O_2$ cell with TEMPO electrolyte. **B.** FTIR spectra and **C.** XRD patterns of the electrodes after cycles. The TEMPO electrolyte was prepared by dissolving 10 mM TEMPO in the DEGDME electrolyte with 0.5 M LiTFSI.

The cycle life of the Li-$O_2$ cell was prolonged with TEMPO electrolyte, compared to the bare DEGDME electrolyte. This is owing to the remarkable capability of TEMPO as a redox mediator to lower the charge over-potentials, which efficiently suppresses parasitic reactions associated with the decomposition of electrolyte solvents at high charge voltage. The use of TEMPO could also accelerate the relaxation of $^1O_2$, which potentially reduces parasitic reactions related to the active oxygen species as well. However, the cell still only lasts for 60 cycles, which is significantly shorter than the one with PDI-TEMPO electrolyte (Fig. 4B). This is due to the additional capability of PDI-TEMPO as a much more efficient superoxide radical quencher to quench superoxide radicals.

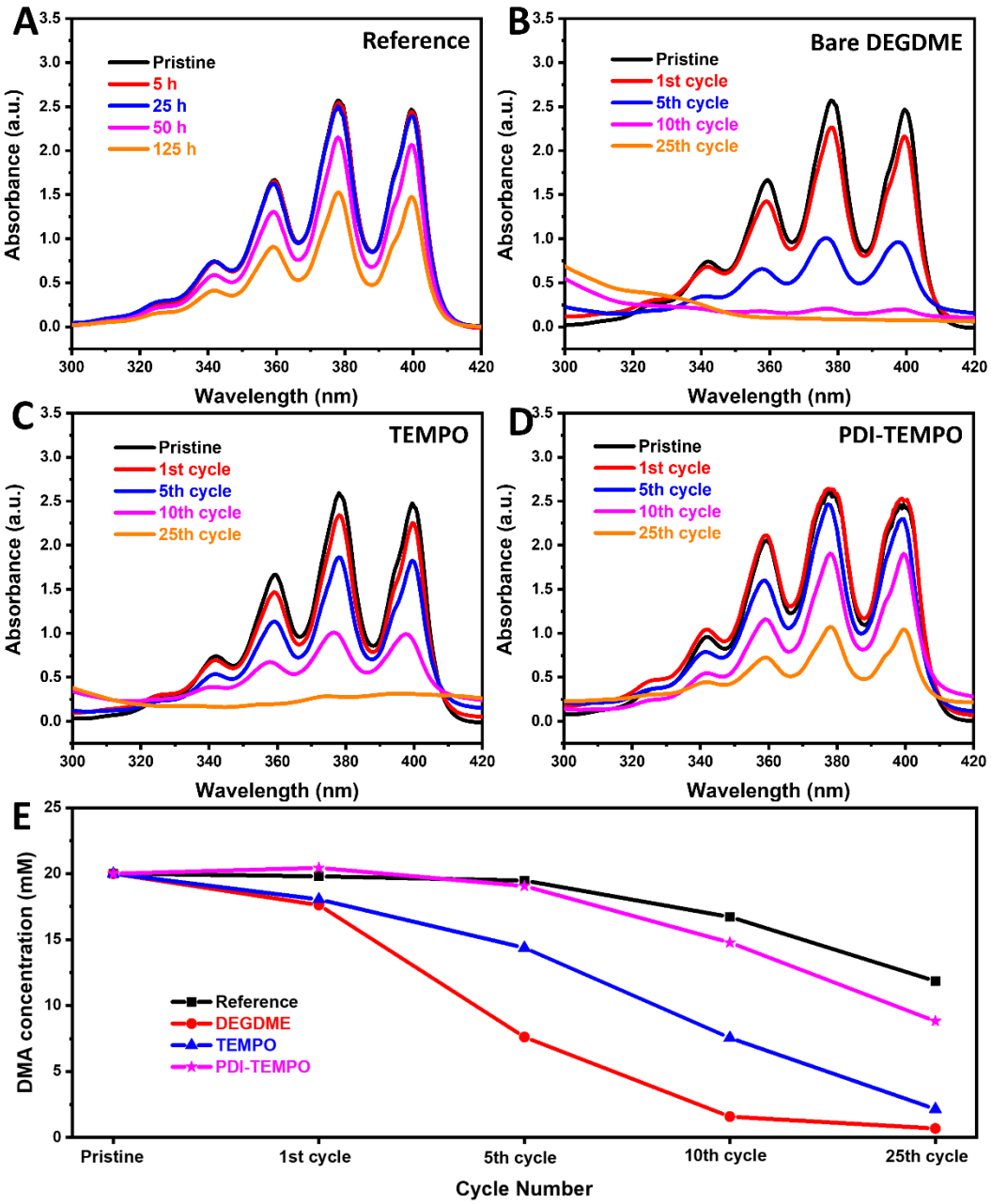


**Fig. S35. Demonstration experiment with 20 mM DMA as the indicator on the suppression effect of singlet oxygen during long-term cycling. a-d.** The UV spectra of **A.** reference and diluted electrolytes retrieved from cells with **B.** DEGDME electrolyte, **C.** 5 mM TEMPO electrolyte, and **D.** 5 mM PDI-TEMPO electrolyte. The reference is 20 mM DMA in DEGDME electrolyte, which rests for a certain time equaling to each cycling period. **E.** The calculated DMA concentration remained in the electrolyte based on the absorbance intensity of peaks at 378 nm. All cells were cycled at a current density of 0.1 mA $cm^{-2}$ with the capacity limitation of 0.25 mAh $cm^{-2}$.

20 mM DMA was dissolved in all three electrolytes includes bare DEGDME, 5 mM TEMPO and 5 mM PDI-TEMPO electrolytes (*41*, *45*, *46*). $LiFePO_4$/C electrodes are used instead of lithium

metal anodes to prevent possible reactions between DMA and lithium metal. The Li-$O_2$ cells with these electrolytes were operated for certain cycles, and all the components retrieved from cells were dissolved in 9 mL pure DEGDME solvent for ultraviolet (UV) tests. A reference was also prepared by resting the bare DEGDME electrolyte with 20 mM DMA under oxygen for the same time of each cycle period to exclude the possible self-degradation of DMA (Figs. S35A and S35E). As shown in Figs. S35B and S35E, the DMA concentration in the bare DEGDME electrolyte shows a sharp drop after each cycle period, indicating a significant amount of singlet oxygen is generated during the operation of Li-$O_2$ batteries. The consumption of DMA in TEMPO electrolyte is much slower than that in the bare DEGDME electrolyte, verifying that the TEMPO can suppress the generation of singlet oxygen owing to its excellent capability in lowing the charge over-potential, and accelerates the relaxation of singlet-state intermediate to triplet-state (Figs. S35C and S35E). Nevertheless, the DMA in TEMPO electrolyte is exhausted before 25 cycles, indicating that singlet oxygen is still generated by parasitic reactions during cycling. Unlike these two electrolytes, the DMA in PDI-TEMPO is consumed much slower, which almost equals the DMA self-degradation rate in oxygen and light (Figs. S35A, S35D and S35E). This result clearly demonstrates that PDI-TEMPO molecules can efficiently suppress the generation of singlet oxygen, by eliminating the origins of singlet oxygen such as quenching superoxide radicals and lowering the charge over-potential, and deactivate singlet oxygen.

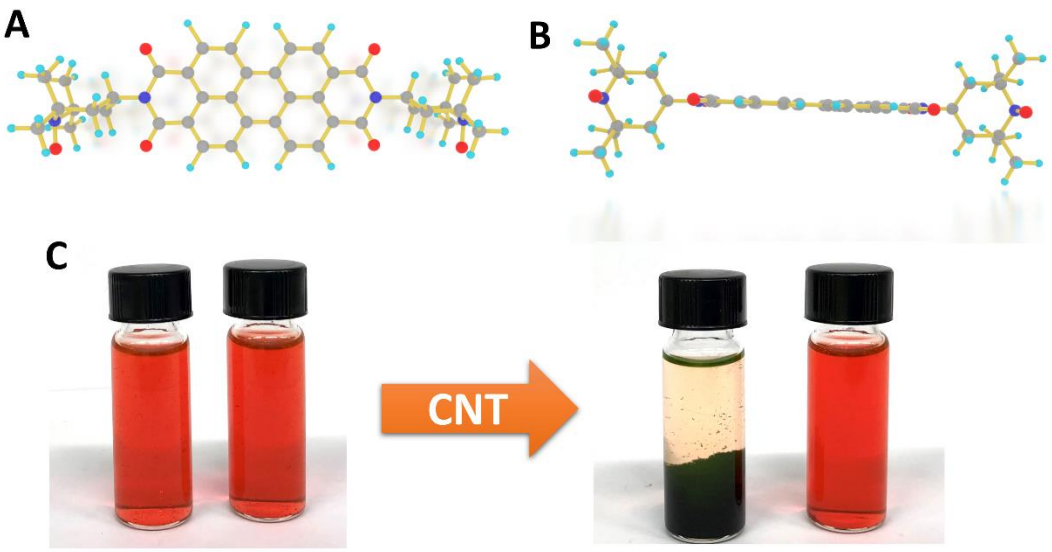


**Fig. S36. The interactions between PDI-TEMPO and CNT electrode. A.** The topview and **B.** sideview of the stereostructure of PDI-TEMPO. **C.** The demonstration experiment by adding CNT in the PDI-TEMPO electrolyte.

The structure of the PDI-TEMPO consists of a conjugated PDI backbone and two TEMPO side functional groups. As shown in Figs. S36A-B, the stereostructure of the TEMPO groups was not in the same plane with the PDI core structure. Instead, they are distributed in a vertical manner, due to the steric hindrance between C=O group from PDI and $CH_2$ group from TEMPO. As a result, the conjugated PDI structure could be easily attracted to the surface of the conjugated graphitic carbon by π-π interactions, while the vertical TEMPO groups could efficiently prevent them from getting too close to the carbon surface to form strong stacking structure. This type of interaction is very critical, as the attraction between PDI and carbon partially restrict the movement of PDI-TEMPO molecules to the cathode side, and the repulsion between TEMPO and carbon could prevent the deposition of PDI-TEMPO molecules to the surface of carbon. A further demonstration experiment was conducted by adding CNT into the PDI-TEMPO electrolyte. It appears that the PDI-TEMPO molecules were drawn to the surface of CNT, leaving the electrolyte with faded colour. It proves that the PDI-TEMPO molecules are restricted to move around the CNT cathode.

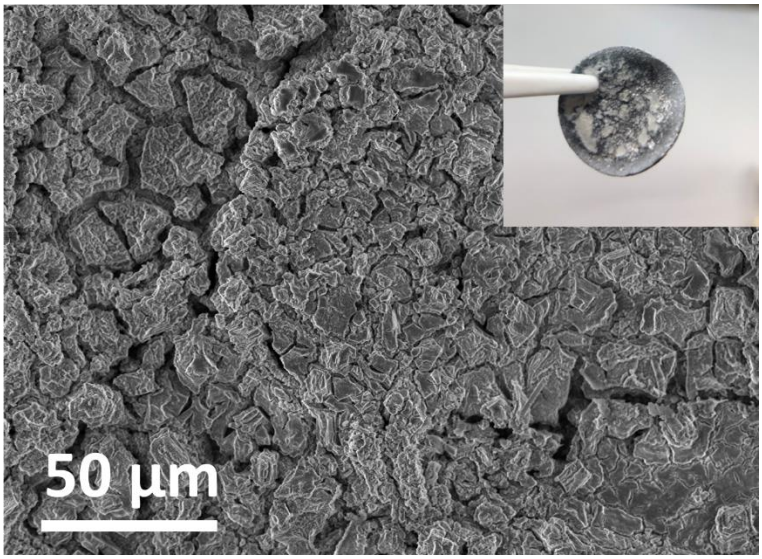


**Fig. S37. SEM image of the lithium metal anode from TEMPO electrolyte after 10 cycles.** The inset image is the digital photo of the lithium metal anode.

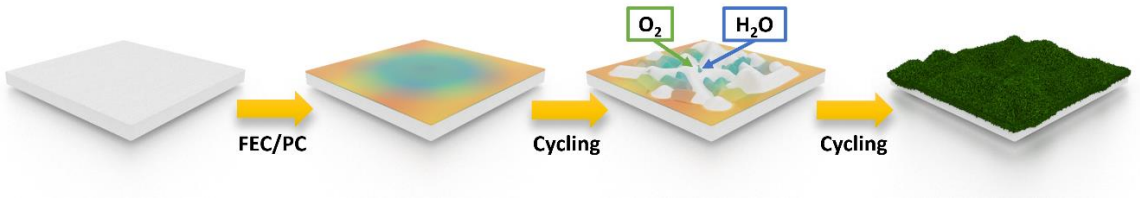


**Fig. S38. The schematic illustration of the corrosion mechanism of lithium metal anode in bare DEGDME electrolyte.**

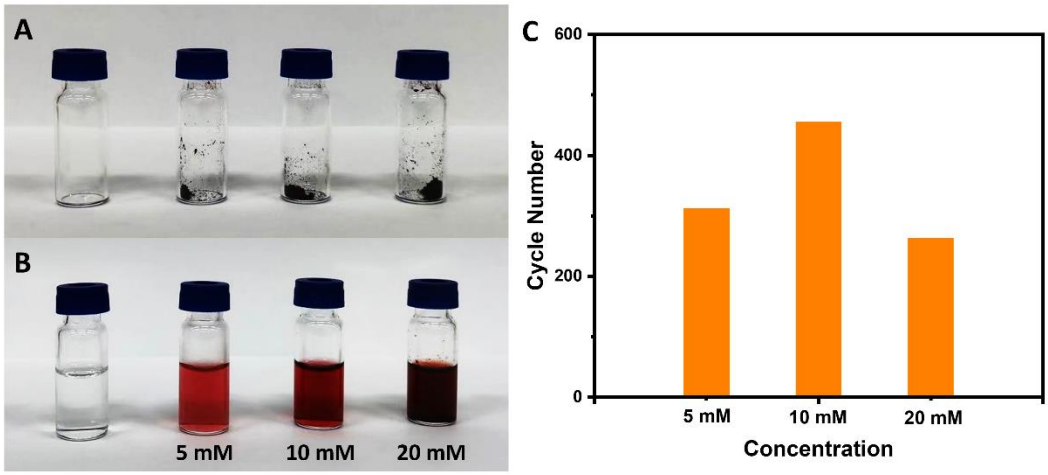


**Fig. S39. Solubility tests and corresponding cycling performance of Li-$O_2$ batteries. A-B.** The digital photo of the electrolyte **A.** before and **B.** after the addition of DEGDME solvent. **C.** The cycling performance of Li-$O_2$ batteries using electrolytes with different PDI-TEMPO concentrations. All cells were cycled at 0.2 mA $cm^{-2}$ with the capacity limitation of 0.25 mAh $cm^{-2}$.

The cell with 10 mM PDI-TEMPO electrolyte achieves the best cycle performance, and the cell with 20 mM electrolyte surprisingly displays fewer cycle numbers than that with 5 mM PDI-TEMPO. This is probably because the high PDI-TEMPO concentration increases the viscosity of the electrolyte, leading to relatively low transport of oxygen and ions. Furthermore, the high concentration of PDI-TEMPO may exceed the capability of graphitic carbon to attract PDI-TEMPO molecules to the cathode, which results in the migration of active molecules to the lithium anode surface. This induces parasitic reactions, which deteriorates the performance of the Li-$O_2$ cell. Therefore, the optimized concentration of PDI-TEMPO in DEGDME solvent is 10 mM.

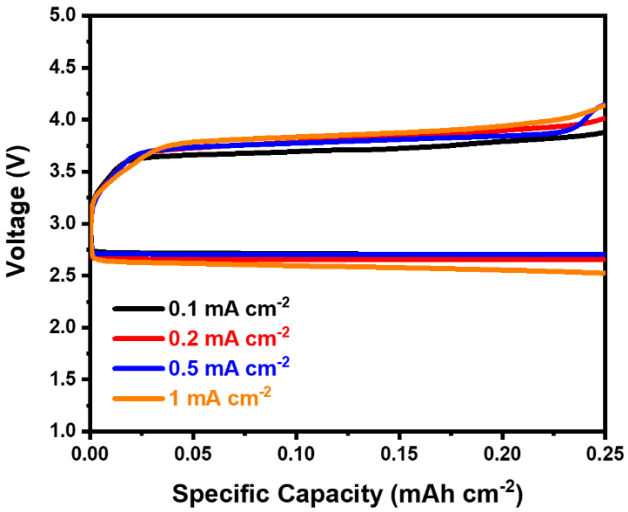


**Fig. S40. Rate capability with PDI-TEMPO electrolyte.** The electrolyte was prepared by dissolving 10 mM PDI-TEMPO in DEGDME electrolyte with 0.5 M LiTFSI.

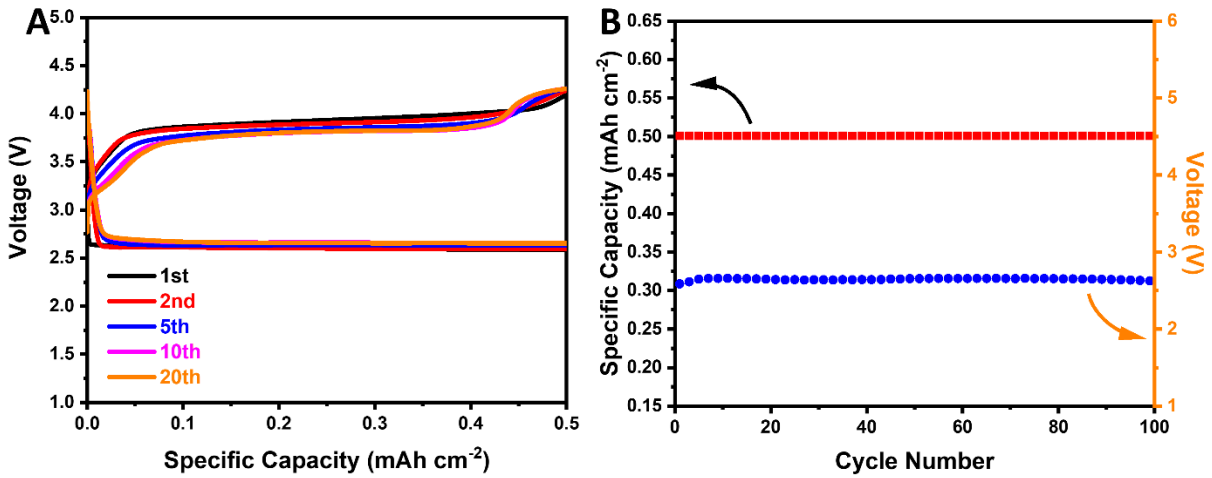


**Fig. S41. A. The discharge-charge profiles and B. cycling performance of the Li-$O_2$ batteries with 10 mM PDI-TEMPO electrolyte at a curtailing capacity of 0.5 mAh $cm^{-2}$.** The current density is 0.2 mA $cm^{-2}$.

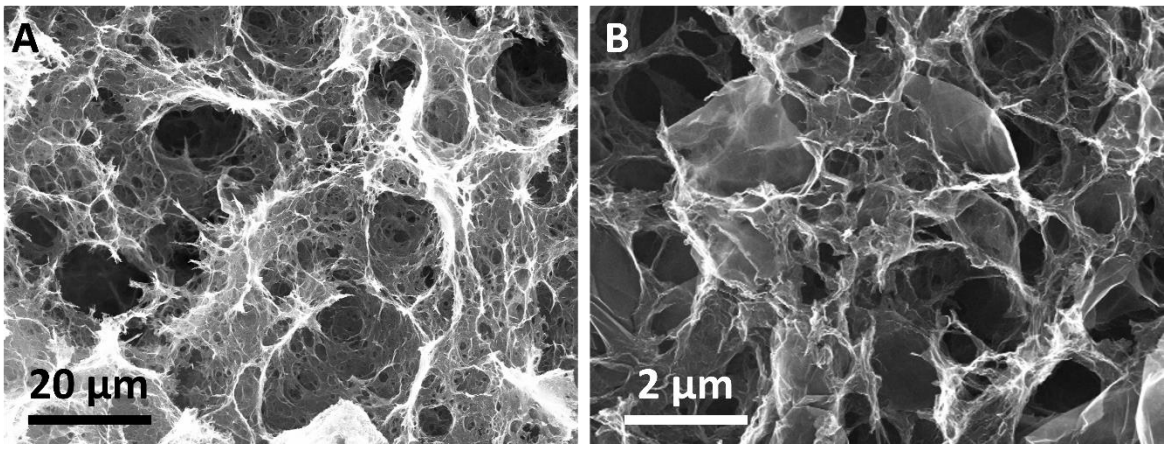


**Fig. S42. The SEM images of porous graphene at A. low and B. high magnifications**.

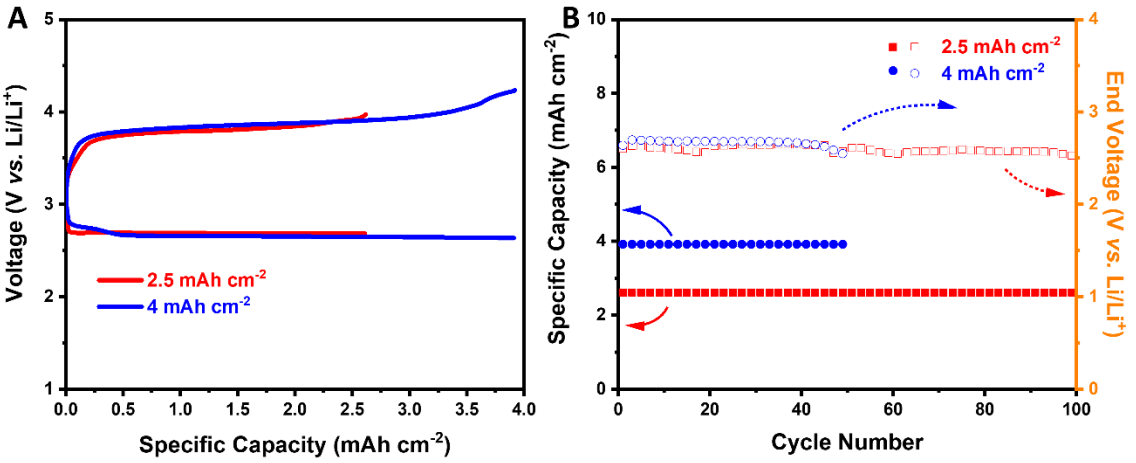


**Fig. S43. The electrochemical performance of Li-$O_2$ battery with 10 mM PDI-TEMPO electrolyte using PGE at high curtailing areal capacities. A.** Discharge and charge curves, and **B.** the cycling performance of Li-$O_2$ batteries with different curtailing capacities. The current density was 0.2 mA $cm^{-2}$ for 2.5 mAh $cm^{-2}$ and 0.5 mA $cm^{-2}$ for 4 mAh $cm^{-2}$.

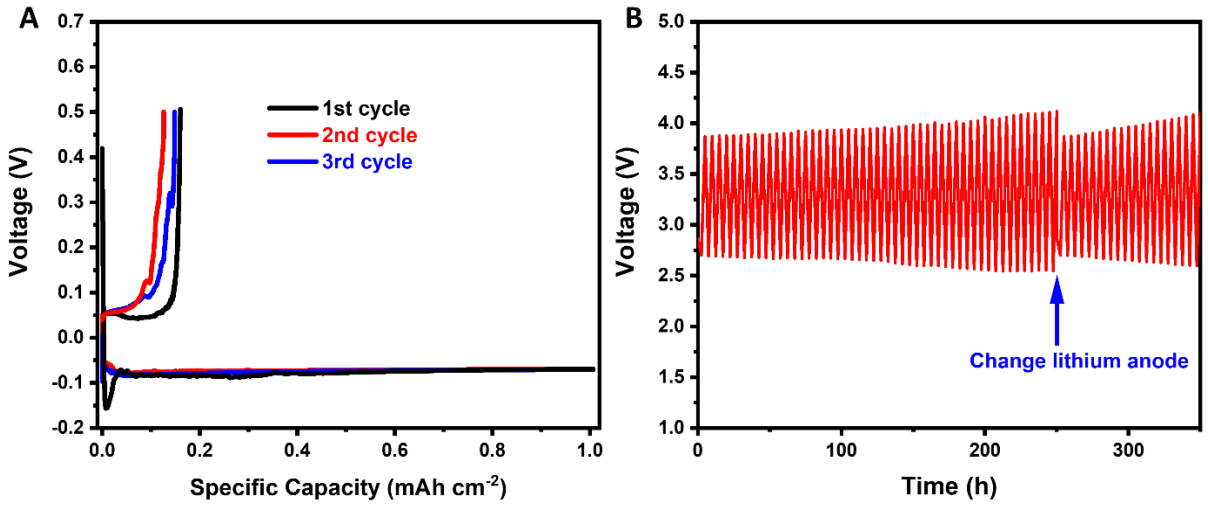


**Fig. S44. The demonstration experiments of lithium metal anode in Li-$O_2$ batteries. A.** The discharge and charge profiles of a Li | Cu half cell. The current density is 1 mA $cm^{-2}$. **B.** The electrochemical performance of Li-$O_2$ batteries before and after the change of fresh lithium metal anode. The current density was 0.1 mA $cm^{-2}$.

Although the unique stereostructure of PDI-TEMPO can efficiently restrict the movement of PDI-TEMPO molecules around the cathode, the parasitic reactions between lithium metal and ether-based electrolyte (forming lithium dendrites, dead lithium, and solid electrolyte interfaces) can still lead to the poor cycling performance of lithium metal anode. To test the cycling stability and Coulombic efficiencies of lithium metal in the bare DEGDME electrolyte, we assembled a Li | Cu half cell using copper foil as the working electrode and bare lithium foil as the counter electrode. Lithium metal was first plated on Cu current collector with a fixed capacity of 1 mAh $cm^{-2}$ and then stripped to 0.5 V at the current density of 1 mA $cm^{-2}$. As shown in Fig. S44A, the half cell shows very low Coulombic efficiencies (<20%). Additional experiment was conducted by replacing the lithium anode after 50 cycles with a fresh lithium metal foil. As shown in Fig. S44B, the over-potential of the Li-$O_2$ cell gradually increases during long-term cycling (250 h). The change of lithium metal anode can efficiently reduce the over-potential of the Li-$O_2$ cell, verifying that the cathode and electrolyte are still active after long-term cycling.

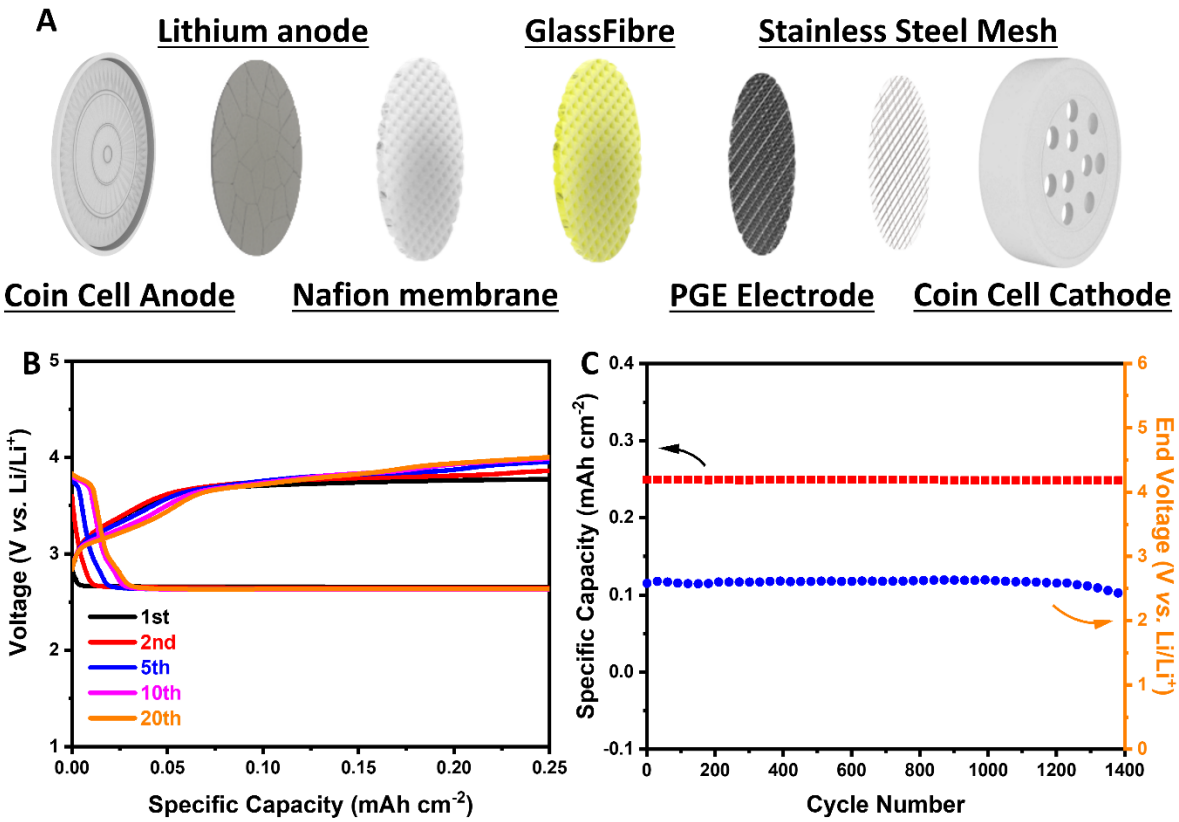


**Fig. S45. The long-term cycling profile of Li-$O_2$ battery with 10 mM PDI-TEMPO electrolyte with PGE and Nafion membrane in the coin cell. A.** The schematic illustration of the coin cell composition. **B.** Discharge and charge curves of the Li-$O_2$ battery and **c.** the corresponding cycling performance. The current density was 0.5 mA $cm^{-2}$.

**Table S1. Comparison of common redox mediators used in Li-$O_2$ batteries**

| Additives | Additional efforts | Calculated reversible capacity* | Accumulated capacity[#] mAh | Cycling number | Reference |
|---|---|---|---|---|---|
| **PDI-TEMPO** | N/A | 0.2 mAh | 90 | 450 | This work |
| **PDI-TEMPO** | Porous graphene | 2/3.2 mAh | 200/160 | 100/50 | This work |
| **PDI-TEMPO** | Nafion membrane/Porous graphene/Coin cell | 0.1 mAh | 140 | 1400 | This work |
| **IL-TEMPO** | N/A | 0.2 mAh | 40 | 200 | Nat. Common. 10, 602 (2019) |
| **TTF** | MoF separator | 0.24-0.33 mAh | 29-40 | 120 | ACS Energy Lett. 3, 463 (2018) |
| **TTF** | Porous graphene | 0.03-0.3 mAh | 3-30 | 100 | Adv. Energy Mater. 7, 1601933 (2017) |
| **TTF** | Porous gold+$LiFePO_4$ | *300 mAh/$g_{gold}$ | N/A | 100 | Nat. Chem. 5, 489 (2013) |
| **TTF** | LiCl+Porous graphene | 0.785 mAh | 78.5 | 100 | Angew. Chem. Int. Ed. 56, 8505 (2017) |
| **LiI** | Polypyrrole | 0.23 mAh | 4 | 17 | APL Mater. 6, 047704 (2018) |
| **LiI** | N/A | 0.5 mAh | 15 | 30 | J. Phys. Chem. C 122, 1522 (2018) |
| **LiI** | N/A | 0.0016 mAh | 0.16 | 100 | J. Mater. Chem. A 3, 8855 (2015) |
| **LiI** | Carbon nanotube array | 0.012/0.036 mAh | 11 | 900/300 | Angew. Chem. 126, 4007 (2014) |
| **LiI** | photoelectrode | 0.6 mAh | 15 | 25 | Nat. Commun. 5, 5111 (2014) |
| **LiI** | Gel polymer electrolyte | 0.096-0.12 mAh | 38-48 | 400 | Angew. Chem. Int. Ed. 56, 7505 (2017) |
| **$LiI(HPN)_2$** | lithiated Nafion membrane | 0.2 mAh | 4 | 20 | J. Phys. Chem. Lett. 8, 4218 (2017) |
| **KI** | N/A | *0.5 mAh $cm^{-2}$ | N/A | 23 | J. Phys. Chem. C 121, 3822 (2017) |
| **CsI** | PEDOT:PSS | ~0.45 mAh | 59 | 129 | ACS Appli. Mater. Inter. 8, 8561 (2016) |
| **$InI_3$** | N/A | 0.19 mAh | 10 | 50 | Energy Environ. Sci. 9, 1024 (2016) |

| | | | | | |
|---|---|---|---|---|---|
| **LiBr** | N/A | *0.5 mAh $cm^{-2}$ | N/A | 40 | Energy Environ. Sci. 9, 2334 (2016) |
| **LiBr** | Solid-state Li-conducting glass-ceramic | *0.4 mAh $cm^{-2}$ | N/A | 15 | J. Am. Chem. Soc. 138, 7574 (2016) |
| **$LiNO_3$** | Bacterial cellulose hydrogel | *500 mAh $g^{-1}$ | N/A | 60 | Carbon 118, 114 (2017) |
| **$LiNO_3$** | N/A | 0.39 mAh | 20 | 50 | RSC Adv. 4, 11115 (2014) |
| **TEMPO** | N/A | *0.35 mAh $cm^{-2}$ | N/A | 10 | ACS Appli. Mater. Inter. 8, 7756 (2016) |
| **TEMPO** | N/A | *0.15-0.25 mAh $cm^{-2}$ | N/A | 50 | J. Am. Chem. Soc. 136, 15054 (2014) |
| **TEMPO** | Composite protective layer | 0.9 mAh | 54 | 60 | Adv. Mater. 28, 857 (2016) |
| **MPT** | $LiFePO_4$ | 0.11-0.15 mAh | 5-8 | 50 | ACS Appli. Mater. Inter. 9, 3733 (2017) |
| **MPT** | $LiNO_3$ | 0.4 mAh | 48 | 120 | J. Mater. Chem. A 5, 10609 (2017) |
| **TMPPA DTBBQ** | Flow cell | 6 mAh | 18 | 3 | ACS Catal. 6, 6191 (2016) |
| **TDPA** | N/A | 0.2-0.3 mAh | 20-30 | 100 | ACS Cent. Sci. 1, 510 (2015) |
| **Viologen LiI** | Redox flow cell | 2 mAh | 60 | 30 | Chem. Commun. 51, 9451 (2015) |
| **1-Me-AZADO** | N/A | 0.314-0.628 mAh | 2-5 | 8 | Phys. Chem. Chem. Phys. 17, 31769 (2015) |
| **FePc** | Graphene sponge | *0.25 mAh $cm^{-2}$ | N/A | 135 | J. Am. Chem. Soc. 136, 8941−8946 (2014) |
| **DBBQ TEMPO** | $LiFePO_4$/ LiSICON | 0.25 mAh | 8 | 50 | Nat. Energy 2, 17118 (2017) |
| **DBBQ TEMPO** | Carbonized polyacrylonitrile electrodes | 0.5 mAh | 10 | 20 | J. Am. Chem. Soc. 140, 1428 (2018) |
| **DMPZ** | PEDOT:PSS | *0.5 mAh $cm^{-2}$ | N/A | 25 | Adv. Energy Mater. 7, 1602417 (2017) |

| | | | | | |
|---|---|---|---|---|---|
| **DMPZ** | N/A | *500 mAh $g^{-1}$ | N/A | 45 | Nat. Energy 1, 16066 (2016) |
| **DMPZ** | FEC+ solid electrolyte membrane | *2000 mAh $g^{-1}$ | N/A | 60 | Adv. Energy Mater. 7, 1701232 (2017) |
| **Heme** | N/A | *600 mAh $g^{-1}$ | N/A | 50 | Nat. Commun. 7, 12925 (2016) |
| **PTIO SDS** | N/A | 0.125 mAh | 19 | 150 | ACS Energy Lett. 2, 2659 (2017) |
| **DMN-AZAD** | Nafion-based $Al_2O_3$ layer | 0.6 mAh | 30 | 50 | ACS Energy Lett. 5, 2122 (2020) |
| **DABCO DMPZ** | N/A | 1.2 mAh | 60 | 50 | ACS Catal. 9, 9914 (2019) |
| **TESI** | N/A | 0.25 mAh | 25 | 100 | Nat. Commun. 10, 3543 (2019) |
| **Vitamin K2 TEMPO** | $LiFePO_4$ | 0.66 mAh | 8.58 | 13 | Adv. Funct. Mater. 29, 1805623 (2019) |
| **hemoglobin** | N/A | *500 mAh $g^{-1}$ | N/A | 20 | J. Phys. Chem. C 123, 23433 (2019) |
| **$V(acac)_3$** | N/A | *500 mAh $g^{-1}$ | N/A | 100 | Angew.Chem. Int. Ed. 58,12553 (2019) |
| **Cu (tdfc)** | Solid electrolyte | 0.45 mAh | 68 | 150 | Mater. Horiz., 7, 214 (2020) |
| **MA-$C_{60}$** | N/A | 0.6 mAh | 36 | 60 | ACS Nano 13, 9190 (2019) |
| **DMPO** | hierarchical CNT electrode | *1000 mAh $g^{-1}$ | N/A | 240 | Adv. Energy Mater. 1904187, (2020) |
| **LiCl** | N/A | 0.8 mAh | 57 | 71 | Batteries & Supercaps (2020) 10.1002/batt.202000198 |
| **DMTFA TEMPO** | High concentration $LiNO_3$ | *1000 mAh $g^{-1}$ | N/A | 100 | ACS Appl. Mater. Inter. 12, 18490 (2020) |

*****Some of the actual capacities cannot be calculated as there is not sufficient information in the publications to perform the calculation.

[#]The accumulated capacity is the total capacity achieved after long-term cycling. The accumulated capacity is calculated by multiplying the reversible capacity by the cycle number.

**Movie S1. The demonstration experiment by adding phenolphthalein into the glassfibre/aqueous electrolyte to prove that the discharge process was mainly accelerated by the chemical disproportion of superoxide radicals.**